International Journal of Solids and Structures 50 (2013) 3009–3026

Contents lists available at SciVerse ScienceDirect

International Journal of Solids and Structures

journal homepage: www.elsevier.com/locate/ijsolstr

Superelastic shape memory alloy cables: Part I – Isothermal tension experiments

Benjamin Reedlunn [a,*], Samantha Daly [b,c], John Shaw [d]

[a] Sandia National Laboratories, P.O. Box 5800, Albuquerque, NM 87185, USA
[b] University of Michigan, Dept. of Mechanical Engineering, 2350 Hayward St., Ann Arbor, MI 48109, USA
[c] University of Michigan, Dept. of Materials Science and Engineering, 2300 Hayward St., Ann Arbor, MI 48109, USA
[d] University of Michigan, Dept. of Aerospace Engineering, 1320 Beal Ave, Ann Arbor, MI 48109, USA

ARTICLE INFO

Article history:
Received 8 June 2012
Received in revised form 19 January 2013
Available online 6 April 2013

Keywords:
Shape memory alloys
Cables
Wire rope
Digital image correlation
Infrared thermography
NiTi
Nitinol
Tensile testing

ABSTRACT

Cables (or wire ropes) made from NiTi shape memory alloy (SMA) wires are relatively new and unexplored structural elements that combine many of the advantages of conventional cables with the adaptive properties of SMAs (shape memory and superelasticity) and have a broad range of potential applications. In this two part series, an extensive set of uniaxial tension experiments was performed on two Nitinol cable constructions, a 7×7 right regular lay and a 1×27 alternating lay, to characterize their superelastic behavior in room temperature air. Details of the evolution of strain and temperature fields were captured by simultaneous stereo digital image correlation and infrared imaging, respectively. Here in Part I, the nearly isothermal, superelastic responses of the two cable designs are presented and compared. Overall, the 7×7 construction has a mechanical response similar to that of straight wires with propagating transformation fronts and distinct stress plateaus during stress-induced transformations. The 1×27 construction, however, exhibits a more compliant and stable mechanical response, trading a decreased force for additional elongation, and does not exhibit transformation fronts due to the deeper helix angles of the layers. In Part II that follows, selected subcomponents are dissected from the two cable's hierarchical constructions to experimentally break down the cable's responses.

1. Introduction

Conventional structural cables (or ropes) are composed of thin filaments of steel, natural or synthetic materials that are helically wound into strands, which in turn are wound around a core. These have long been used as structural tension elements for a variety of applications. For example, steel wire rope is used in civil engineering structures for power cables, bridge stays, and mine shafts; in marine and naval structures for salvage/recovery, towing, vessel mooring, yacht rigging and oil platforms; in aerospace structures for light aircraft control cables and astronaut tethering; and in recreation applications like cable cars and ski lifts.

Structural cable is a built-up structure assembled in a hierarchical manner from thin wire elements (see Fig. 1(a)). Several wires, not necessarily of the same diameter, are helically wrapped around a single wire to form a strand. Several strands are then laid helically around an axial core, which laterally supports the outer strands to create a nominally circular cross-section. Depending on the application, the axial core can be another strand, natural fibers, or a polymer. The chirality, or handedness, of both the wires in a strand and of the strands in a rope can be laid in an opposite sense (regular lay) or same sense (lang lay), which affects the helix angle the wires make with the cable axis (Fig. 1(b)) and the tension–torsion coupling of the overall cable response.

As a structural tension element, wire cable has many desirable qualities. It is relatively stiff in uniaxial tension and often has a large tensile strength, yet it is compliant in torsion and bending due to the large aspect ratio of the rope and the helical lays of elements within the cable. This compliance enables ease of handling and spooling. The numerous wires and strands support the tensile load in parallel, providing redundancy and more forgiving failure modes, since the failure of one wire does not necessarily propagate to the failure of other wires, unlike fracture across a monolithic bar. The strand and rope cross-sections can be constructed in various geometric patterns, leading to considerable design flexibility with respect to axial stiffness, stored elastic energy, bending/twisting compliance, exterior smoothness, abrasion resistance, and redundancy.

Shape memory alloys (SMAs), such as NiTi-based alloys (including Nitinol), exhibit two remarkable properties, the *shape memory effect* and *superelasticity*. The shape memory effect is the material's ability to recover large mechanically-induced strains upon heating

* Corresponding author. Tel.: +1 505 284 9677.
E-mail addresses: breedlu@sandia.gov (B. Reedlunn), samdaly@umich.edu (S. Daly), jashaw@umich.edu (J. Shaw).

0020-7683/$ - see front matter © 2013 Elsevier Ltd. All rights reserved.
http://dx.doi.org/10.1016/j.ijsolstr.2013.03.013

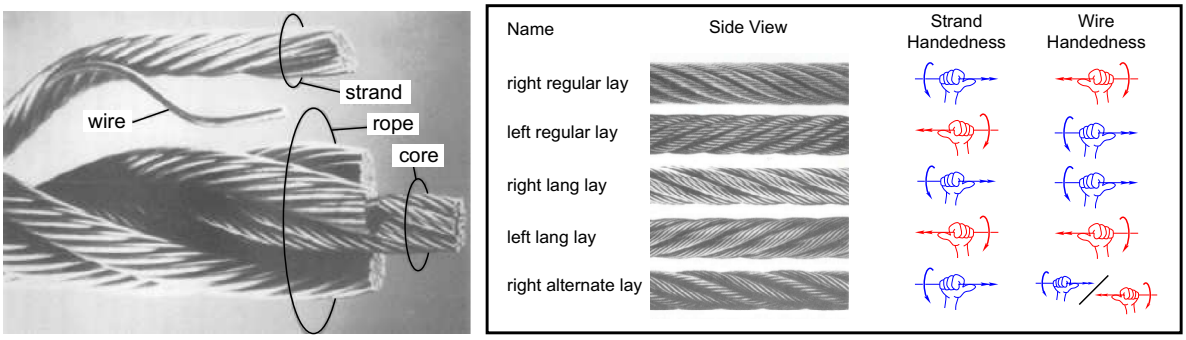

(a) Typical wire rope construction (b) Typical wire rope lays

Fig. 1. Wire rope terminology (adapted from McKenna et al. (2004) and Costello (1998)).

above a transition temperature. Superelasticity (or pseudoelasticity) refers to the material's ability, above a transition temperature, to recover strains isothermally during a mechanical load/unload cycle, usually via a hysteresis loop. The tensile strain recovery in a Nitinol polycrystal is between 5 and 8% in the low-cycle limit and near 2.5% in the high cycle fatigue limit. These properties can be exploited to generate/withstand large stresses (several hundred MPa) and moderately large strains (for a metal), giving rise to a mechanical energy density orders of magnitude larger than other typical actuator systems and adaptive materials, like piezoelectric, electrostrictive, magnetostrictive, and ferromagnetic materials (Huber et al., 1997). This potentially enables more compact structural designs than would otherwise be possible. These properties and others, such as Nitinol's high tensile strength, corrosion resistance and biocompatibility, have made Nitinol the most popular SMA. NiTi is used in a growing number of engineering, consumer, and biomedical applications (Funakubo, 1987; Duerig et al., 1990; Otsuka and Wayman, 1998), and it is being investigated for use in novel structural elements (Semba et al., 2005; Shaw et al., 2007).

The underlying mechanism for the shape memory effect and superelasticity is a reversible, temperature-induced or stress-induced martensitic transformation between solid-state phases. This transformation often occurs near room temperature in Nitinol. At zero stress, the high temperature phase is called austenite (A), which has a B2 (cubic) crystal structure, and the low temperature phase is called martensite (M), which has a low symmetry monoclinic B19' structure (Otsuka et al., 1971) with 12 energetically equivalent lattice correspondence variants. Due to its low degree of symmetry, the martensite phase can exist in a variety of microstructures either as a randomly oriented/twinned structure (low macroscopic strain) or a stress-induced oriented/detwinned structure (denoted macroscopically here as M^+ in tension) that can accommodate relatively large, reversible strains. The transition temperatures of the material can be tailored to the user's specification by the alloy chemistry and thermo-mechanical processing, so at room temperature the material can be either a shape memory material (austenite above room temperature) or a superelastic material (austenite at room temperature).

Exploratory experiments have been presented by the authors in conference papers (Reedlunn and Shaw, 2008; Reedlunn et al., 2009) on two different commercially available Nitinol cable constructions. The articles in this two part series summarize the important aspects of these conference papers and present new experiments on the same two cable designs. Our primary aim is to present detailed experimental thermo-mechanical data and explain the observed phenomena. Structural and constitutive modeling, a challenging task, is left for future work.

The remainder of this paper (Part I) is organized as follows. Section 2 provides a further discussion of the technical and scientific motivation for this study. Section 3 describes the geometry of the two cable designs and specimen preparation. Section 4 details the experimental setup. Section 5 contains the experimental results, and Section 6 provides a summary of results and conclusions.

2. Motivation for study

SMA cables are a relatively new class of structural elements that (1) inherits many of the advantages of conventional wire rope, (2) adds new adaptive functionality (shape memory and super elasticity) to structural cables, and (3) leverages the excellent properties of thin SMA wire into large force tension elements. Wire ropes are relatively damage resistant, since failure of a single wire in a multiwire bundle has less dramatic consequences than fracture in a monolithic bar. They represent a class of structures with large design flexibility, due to the myriad of possible filament diameters, cross-section sizes, cross-section geometries, and lays of individual components. They are relatively stiff in tension, yet flexible in bending and torsion, resulting in ease of handling and excellent fatigue performance under cyclic flexure compared to solid wires/bars of the same overall cross-sectional area. In a recent study, Redmond et al. (2008) spooled shape memory wires to generate a large stroke actuator in a compact package. SMA cable actuators can be spooled more tightly than monolithic SMA wires of the same overall diameter. Thus cables enable either a more compact spooled actuator with the same force, or a larger force actuator with the same footprint.

Due to their underlying shape memory and superelastic properties, cables made of SMAs have potential performance advantages over conventional metal cables. Under impact loading, steel cable is susceptible to "birdcaging", which is a bulbous-like permanent deformation mode that involves kinking of individual wire elements. This is caused by excessive compression (often resulting from a dynamic event), and usually leads to scrapping of the cable (Costello, 1998). SMA cables, on the other hand, are relatively kink-resistant and transient overloading is less likely to incur permanent damage. The transformation plateaus in the superelastic behavior could be used to design cables that have inherent overload protection for adjacent structures and large energy absorption capabilities under impact loading. Furthermore, SMA cables can exhibit the shape memory effect across a threshold temperature, so they can be made to act as thermal actuators.

The construction of SMA wire rope is a promising way to resolve longstanding impediments in realizing large-force SMA elements. Historically, producing complex shapes by joining Nitinol to itself

or to adjacent materials has been difficult. In the past, joining Nitinol has required specialized welding techniques, complex laser machining, or mechanical crimping, although recent progress has been made on alternative joining techniques (Grummon et al., 2006; Shaw et al., 2007)). Furthermore, as a monolithic material, Nitinol does not scale up easily for several reasons:

- Properties of large-section bars are generally poorer than those of wires due to difficulties in controlling quench rates through the section during material processing and the impracticality of cold work procedures that have been optimized for SMA wire (although again, some recent improvements have been made, see DesRoches and McCormick, 2003; Frick et al., 2005; Ortega et al., 2005).
- The thermal response time, due to the strong thermo-mechanical coupling, scales with the volume-to-surface ratio, leading to a sluggish response in large monolithic SMA bars.
- Large bars of Nitinol are quite expensive. Currently, a 6.35 mm diameter bar is about $400/m, while a conventional 49-wire Nitinol cable of equal outer diameter ($7 \times 7 \times 0.711$ mm, using the naming convention in Section 3) is only $60/m (Ft. Wayne Metals, 2012).

By leveraging the highly optimized manufacturing processes currently available for wire, the cable form results in a large-force SMA element with superior properties for substantially less cost than a monolithic bar of comparable size.

Since SMA in cable form is a relatively new concept, SMA cables have only been implemented in few applications to date. In biomedical applications, small-scale stranded SMA wire is currently used where tight bend radii and high resistance to cyclic bending fatigue are needed. For example, small diameter superelastic strands are used for dental files due to NiTi's high hardness and the strand's ability to flex through tortuous cavities. Similarly, stranded SMA wire is used for vascular filters, snares, and guidewires for its ability to navigate the severe twists and turns of the vascular anatomy (Ft. Wayne Metals, 2010). In fact, recent fatigue cracks in the electrodes (lead wires) of implanted heart devices (Meier, 2007) may make SMA cables an appealing alternative for this application. SMA wires do cost four to eight times more than stainless steel wires, but material costs are often a small fraction of the total price of a biomedical device, so this is not a large barrier to commercialization. In the consumer sector, superelastic cables have seen use as cell phone antennas that can withstand extreme handling (Ft. Wayne Metals, 2010).

A number of (primarily applications oriented) publications exist in the open literature where researchers have exploited certain features of SMA cables. Intense interest exists in the US and Europe to use large SMA elements, including cables, for vibration suppression and seismic protection of civil engineering structures. In another civil engineering application, Song et al. (2006) embedded pre-stretched martensitic SMA cables in concrete, and post-tensioned the cables via joule heating to prestress concrete in compression. We expect that SMA cables could be used as reinforcements in other composites, where the rough exterior of the wire rope would help mitigate some long-standing debonding problems between the SMA and matrix material. SMA cables were also investigated as actuation elements in a full-scale prototype of a variable area fan nozzle for the next generation of high bypass turbofan jet engines (Rey et al., 2001; Barooah and Rey, 2002). Beyond these existing and proposed applications, we believe SMA cables could have significant future promise as high-force actuators, thermal latches, and shock absorbing devices, which could be useful for a number of future infrastructure and transportation applications. They could be used as thermally-active structural members in a shape memory mode or as extremely resilient elements in a superelastic passive mode. Despite these advantages, we are not aware of any detailed characterization studies of SMA cables in the open literature. This series of papers aims to start filling that void.

Besides the technological implications, SMA cables have scientifically interesting properties. Rich thermo-mechanical coupling and phase transformation-induced instabilities occur even in simple, uniaxially loaded SMA wires and strips (Shaw and Kyriakides, 1995, 1997, 1998; Chang et al., 2006; Liu et al., 1998; Sun et al., 2000). Built-up cables add multi-scale material–structural interactions, where contact conditions and latent heat interactions between adjacent wires can cause complex patterns of transformation kinetics. Many elaborate SMA constitutive models have been proposed in recent decades, but few have been validated against multi-axial experiments. The opportunity to investigate SMA constitutive behavior under complex stress states arising from inherent combined tension–torsion-bending is an additional scientific motivation to characterize SMA in wire rope form.

3. Specimens

Two NiTi cable designs were obtained from Fort Wayne Metals, Research Products Corp. (Fort Wayne, Indiana). Fig. 2 shows annotated photographs of the $7 \times 7 \times 0.275$ mm design (right regular lay), as well as a less conventional $1 \times 27 \times 0.226$ mm cable made from slightly thinner wires. The identifier $7 \times 7 \times 0.275$ mm indicates the number of strands, the number of wires in each strand, and the wire diameter, respectively. Fort Wayne Metals shape set the cable constructions by heat treating the specimens at roughly 500 °C for a few minutes while the wires were mechanically constrained. As a result, the wires do not unravel if the cables are dis-

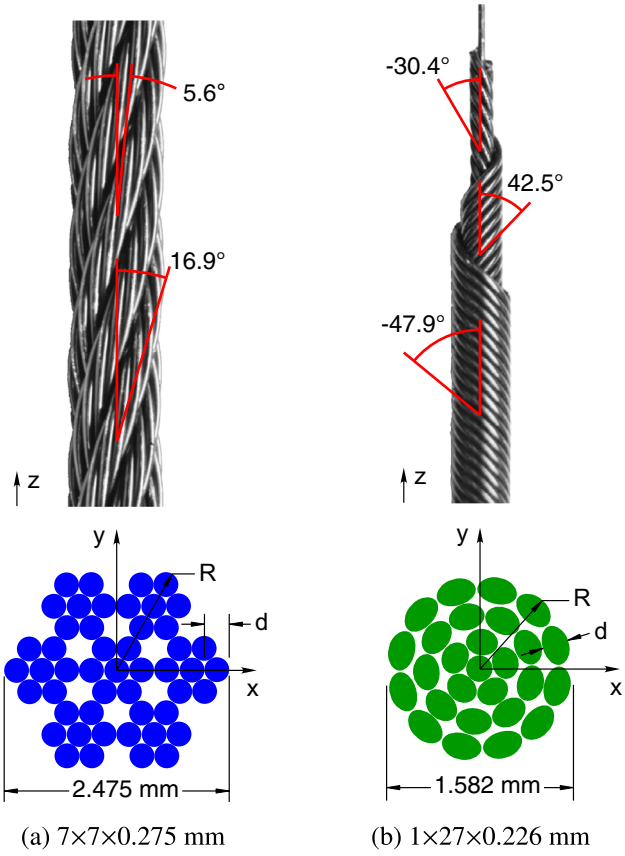

Fig. 2. Two NiTi cable designs, showing side views (upper photographs) and cross-sections (lower schematics).

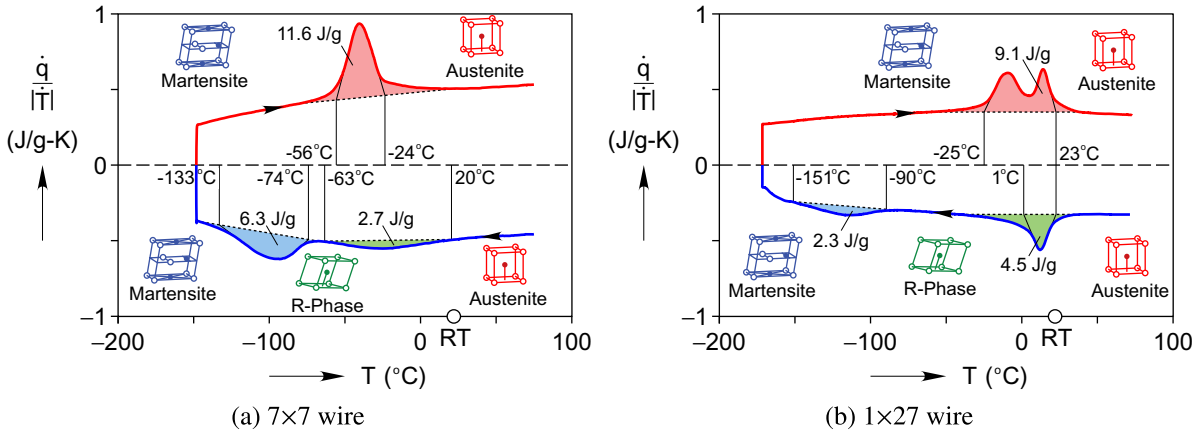

(a) 7×7 wire (b) 1×27 wire

Fig. 3. Differential scanning calorimetry thermograms.

assembled. All wires in each cable design came from a single wire manufacturing lot and experienced the same nominal heat treatment. Thus, the wire properties should be relatively uniform throughout a given cable. Each experiment described in Section 5 and in the subsequent parts was performed on a new specimen, as-received from the manufacturer.

3.1. Cable geometry details

Fig. 2 shows cross-section schematics and side view photographs of the two cable designs, including the measured cable diameters and helix angles[1] (α_0) of individual wires to the cable's global axis (z-axis). The helix angles reported in Fig. 2 differ by a few degrees from those reported in our previous conference papers (Reedlunn and Shaw, 2008; Reedlunn et al., 2009; Reedlunn et al., 2010), where the helix angle was estimated from digital photographs of the specimens. Here, we measured the reference helix pitch (p_0) and mean helix diameter (D_0, to the wire centerline) under a microscope with a micrometer translation stage to calculate the reference helix angle by $\alpha_0 = \tan^{-1}(\pi D_0/p_0)$. The pitch was measured by averaging the linear distance of at least seven helical turns, resulting in a more accurate measurement.

The first (7×7) cable design is a traditional right regular lay, where the six exterior strands are wound in a right-handed helix ($\alpha_0 = 16.9°$) around the core strand (Fig. 2(a)). The core strand consists of six wires wound in a right-handed helix ($\alpha_0 = 11.3°$, not shown in Fig. 2(a), but see Part II) around the straight core wire ($\alpha_0 = 0°$). An exterior strand consists of six wires wound in a left-handed sense (varying with position, $5.6° \leqslant \alpha_0 \leqslant 28.2°$) about a central helical wire ($\alpha_0 = 16.9°$).

The second (1×27) cable design is more tightly wound and was selected to provide a comparison with the previous design. Strictly speaking, it is a single layered strand, not a multi-strand cable, yet for brevity we will call it a cable. The outer layer portions of the 1×27 cable were removed to reveal the alternating helices shown in Fig. 2(b). The center core wire is straight ($\alpha_0 = 0°$). Progressing radially outward, the next three helical layers are composed of 5 wires at $\alpha_0 = -30.4°$, 9 wires at $\alpha_0 = 42.5°$, and 12 wires at $\alpha_0 = -47.9°$, respectively.

3.2. Material calorimetry

The transformation temperatures of a 7×7 wire and a 1×27 wire were measured by a Perkin–Elmer Pyris 1 differential scanning calorimeter (DSC) or a TA Instruments Q2000 DSC, respectively. Material specimens were prepared as outlined in Shaw et al. (2008). The endothermic heat flows (vertical axes) shown in the thermograms of Fig. 3 are normalized by the specimen mass (30.93 mg and 18.48 mg, respectively, for the 7×7 and 1×27 wires) and the temperature scan rate of ± 10 °C/min. Indium was used as a reference material to calibrate the temperature and heat flow. Both materials exhibit a two step transformation from A to rhombohedral phase (R) and then $R \rightarrow M$ during cooling, as is common for commercial Nitinol. During heating, the 7×7 material (Fig. 3(a)) has overlapping $M \rightarrow R$ and $R \rightarrow A$ transformations creating a single peak, while the 1×27 (Fig. 3(b)) has partially separated $M \rightarrow R$ and $R \rightarrow A$ transformations. The austenite (A_s and A_f), martensite (M_s and M_f) and rhombohedral (R_s and R_f) transformation temperatures are indicated on the thermograms, as well as the corresponding specific enthalpies of transformation. The 7×7 material is clearly superelastic at room temperature since $A_f = -24$ °C. The double peak for the 1×27 during heating makes it somewhat less clear, but the mechanical response at room temperature (shown later in Fig. 6(b)) confirms that the material is indeed a superelastic alloy, and we estimate remains superelastic down to about 10 °C.

3.3. Specimen preparation

During the experiments, the average axial strain of a large central gage section was measured by a laser extensometer (LE), and the local axial strain distribution was measured by stereo digital image correlation (DIC) in a selected region of interest. DIC is used to measure full-field surface displacements of an object by tracking the specular pattern on the surface of a specimen (Sutton et al., 2009). Both LE and DIC are optical, non-contact techniques that required special specimen preparation. For LE measurements, two retro-reflective tags were attached to the specimen, and the current length between them was measured by the LE by projecting a planar (vertical) laser sheet along the specimen length. A minimum LE tag width (horizontal) of at least 1.2 mm was required to get a reliable reading. LE tags were directly attached to the surface of sufficiently thick specimens, but epoxy tabs were made to affix LE tags for specimens less than 1.2 mm in diameter. For DIC, once the epoxy had cured, the specimen was airbrushed with a background coat of Golden Airbrush Titanium White (#8380), followed by a speckle coat of Golden Airbrush Carbon Black (#8040). The resulting speckle pattern is shown in Fig. 4(b) on a core wire extracted from a 1×27 cable. The magnified image is a portion of the actual image used for the DIC analysis, which shows 47 pixels across the wire diameter and a typical 19×19 subset used in

[1] Note that α_0 is measured here from the loading axis (z-axis), which is the complement of the angle conventionally used for helical springs (measured from a lateral axis).

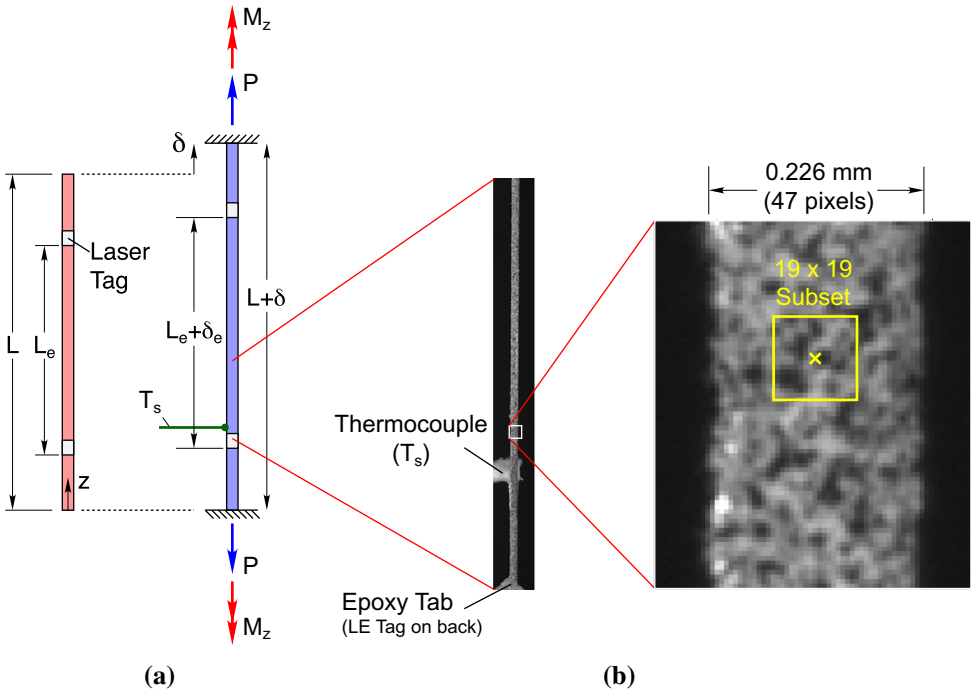

Fig. 4. (a) Specimen schematic and free body diagram, (b) photograph of DIC field of view and close up of the speckle pattern on a 1×27 core wire.

the correlation analysis. More details on the specimen preparation procedure can be found in Reedlunn et al. (2013).

4. Experimental setup

The experimental setup shown in Fig. 5 provided elongation-controlled tensile testing of SMA cable specimens and their selected components in room temperature air. The evolution of axial load, axial torque, axial strain and temperature were measured during the experiments. A list of these measurements, along with estimates for their uncertainties, are provided in Table 1. The specimen was oriented vertically as shown near the center of the photograph in Fig. 5(a). The specimen ends were clamped between hardened steel plates within pneumatically-actuated grips, resulting in an axial free length of $75 \leqslant L \leqslant 90$ mm. Specific specimen dimensions and other parameters for each experiment of this article are listed in Table 2. The specimen was loaded uniaxially in displacement control by an Instron 5585 electro-mechanical,

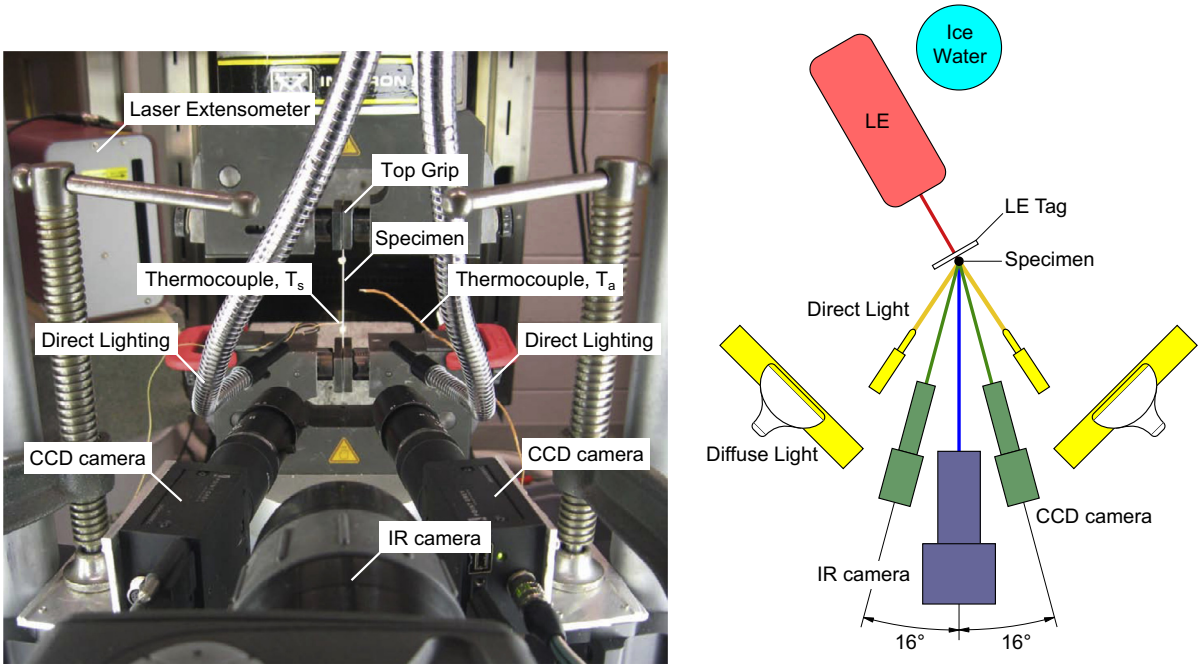

(a) Front view photograph (b) Top view schematic

Fig. 5. Experimental setup.

Table 1
Measured quantities and their uncertainties.

Variable	Description	Calibration range	Uncertainty estimate
δ	Upper grip displacement	50 mm	±0.005 mm
δ_e	Laser extensometer elongation	20 mm	±0.01 mm
P	Axial load	500 N or 5 kN	±0.25% of reading
M_z	Reaction torque	2824 N-mm	±5 N-mm
T_s	Specimen thermocouple	0–100 °C	±0.5 °C
T_a	Ambient air thermocouple	0–100 °C	±0.5 °C
T	IR temperature field	−10–50 °C	±0.5 °C
E^L	DIC strain field	N/A	±0.1% Local strain
			±0.02% Average gage length strain

Table 2
Experimental matrix and parameters.

Specimen	Icon	D (mm)	Exp ID	Condition	L (mm)	L_e (mm)	Cycles	$\dot{\delta}/L$ (s^{-1})
7 × 7 × 0.275 mm	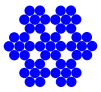	2.475	C1a	Dry	77.33	50.30	1	$\pm 2.5 \times 10^{-5}$
			C1b	Lubricated	76.18	49.76	1	$\pm 2.5 \times 10^{-5}$
			C1c	Dry	74.85	49.92	1	$\pm 1 \times 10^{-5}$
			C1d	Dry	82.21	50.58	6	$\pm 1 \times 10^{-4}$
7 × 7 core wire	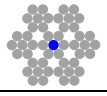	0.275	W1a	–	85.90	52.70	6	$\pm 1 \times 10^{-4}$
1 × 27 × 0.226 mm		1.582	C2a	Dry	80.87	49.90	1	$\pm 1 \times 10^{-4}$
			C2b	Lubricated	86.73	50.56	1	$\pm 1 \times 10^{-4}$
			C2c	Dry	89.33	50.81	6	$\pm 1 \times 10^{-4}$
1 × 27 core wire		0.226	W2a	–	75.09	49.12	6	$\pm 1 \times 10^{-4}$

lead-screw driven, load frame, where the lower grip was fixed and the upper grip displacement (δ) was controlled and measured by the load frame's high resolution optical encoder. The resultant axial force (P) was monitored by a 500 N (Instron model 2525–816) or 5 kN (Instron model 2525–805) load cell, depending on the specimen size. The chiral architecture causes the cable to naturally unwind as it is stretched along its axis if one end is free to rotate. Here, however, the ends of the cable were rigidly clamped, preventing rotation about the z-axis, so a 2824 N-mm capacity torque cell (Futek TFF400) was added beneath the lower grip to measure the axial torque (M_z) in many of the experiments. All experiments were performed in elongation-control, where the upper grip displacement $\dot{\delta} = d\delta/dt$ was prescribed at a constant rate during loading ($\dot{\delta} > 0$) and unloading ($\dot{\delta} < 0$).

Temperature was monitored simultaneously by discrete thermocouples and full-field infrared (IR) measurements. Two K-type thermocouples, one placed near the specimen and one attached to the specimen, measured the ambient air temperature (T_a) and the specimen temperature (T_s). The specimen thermocouple was located just above the lower LE tag (see Fig. 4a), and a small amount of thermally conductive paste (Omegatherm 201) was applied to the specimen thermocouple to ensure good thermal contact with the specimen. The entire axial temperature field $T(z)$ of the front of the specimen was measured by an Inframetrics ThermCam SC1000 radiometer having a 256 × 256 pixel array. The emissivity of the painted specimen was measured to be $\epsilon = 0.91$ (sufficiently close to the ideal emissivity of 1) by comparing the infrared temperature reading against the specimen thermocouple. A container of ice/water was placed about 0.6 m behind the specimen (see Fig. 5(b)) to provide background contrast in the infrared images. A fine-meshed (mosquito) netting was also draped over the entire experimental setup to ensure that the specimen was surrounded in stagnant air and avoid any stray air currents. The ice/water container and fine-mesh netting was removed for the photo in Fig. 5(a) to avoid obscuring the setup.

The specimen strain was measured by both laser extensometry and stereo DIC to provide average strain and local strain-field measurements, respectively. Both methods provide accurate, non-contact strain measurements that have been previously confirmed to give good agreement (Reedlunn et al., 2013). A laser extensometer (Electronic Instruments Research model LE-05) measured the elongation (δ_e) between affixed laser tags. The tags typically spanned a length of $L_e \approx 50$ mm in the central portion of the specimen gage section. The laser extensometer (LE) shown in Fig. 5 was placed behind the specimen to avoid shining the laser sheet on the front side of the specimen, which would interfere with optical imaging for DIC. Since DIC produces full field strain data, it might appear that the LE is unnecessary, but we found it useful for several reasons in addition to its use as a confirmatory measurement. The LE provided real-time strain measurement as the experiment progressed, could be collected at a moderately high rate (12.5 Hz after oversampling/averaging) without excessively large data files, was easily integrated into the load frame control software, and measured the axial strain over a larger axial length than the DIC field of view. Also, while the elongation was prescribed by the grip displacement, the maximum elongation for a given load-unload cycle was selected and controlled by the LE measurement. Artifacts from grip slippage (typically unavoidable in such setups when transformation fronts, i.e. localized strains, entered or exited the free length) were eliminated in the mechanical responses by reporting the gage strain from the laser extensometer (δ_e/L_e) or DIC [2] ($\mathbf{E}^L$) rather than the global strain (δ/L). Furthermore, it is well known that

[2] The default strain measure of our DIC software was the Green–Lagrange strain, $\mathbf{E}^L \equiv \frac{1}{2}\left[\left(\mathbf{F}^T \cdot \mathbf{F}\right) - \mathbf{I}\right]$, where $\mathbf{F} \equiv \partial\mathbf{x}/\partial\mathbf{X}$ is the deformation gradient and $\mathbf{I}$ is the identity tensor.

the prescribed "global strain rate" is quite different than the "local strain rate" during transformation front propagation.

Optical imaging for stereo DIC was performed from the front of the specimen as shown in Fig. 5(b). The two CCD cameras shown on either side of the infrared camera in Fig. 5(a) are Pt. Grey Research Grasshoppers (GRAS-50S5M-C). Each is a compact camera with a 2448×2048 (3.45 μm square pixels) grayscale CCD. The manufacturer reports the Grasshopper is capable of 14 bit grayscale resolution, but the effective (noise free) dynamic range was about 8 bits for our setup. The aperture diameters of the Tamron CCTV 75 mm focal length lenses shown in Fig. 5(a) were set to 9.4 mm or 12.5 mm depending on the experiment. The exposure time ranged from 50 ms for slow rate experiments ($\dot{\delta}/L \leqslant 10^{-4}\ \mathrm{s}^{-1}$) to 2.7 ms for higher rate experiments ($\dot{\delta}/L = 10^{-2}\ \mathrm{s}^{-1}$), which gave less than 0.1 pixel of specimen movement during the exposure. Considering the temperature sensitivity of NiTi, special care was taken to choose lighting sources that did not affect the specimen temperature. We used fluorescent lights behind frosted translucent plastic (just out of view in Fig. 5(a)), similar to a photographer's light box, to produce a diffuse, flat light. In addition, flexible fiber optic lights (extending in from the top of Fig. 5(a)) with an adjustable light intensity were used to finely adjust the illumination. Care was also taken not to shine the fiber optic lights directly at the LE, which would affect the extensometer reading.

While the IR camera measured the temperature field across the entire specimen length, the DIC region in Fig. 4(b) included only a portion of the specimen length. The IR camera can measure the temperature of a wire only one pixel wide when calibrated and aligned properly, but DIC requires many pixels across the specimen's diameter to calculate strains accurately. In preliminary calibration tests, we found that a minimum of 35 pixels across a straight wire was needed to properly resolve the axial strain for DIC, so 47 pixels was selected to be conservative. Thus, although the diameter of the cable was 1.58 mm or 2.48 mm, the DIC FOV was limited by the camera resolution and the diameter of the individual wires (0.226 mm or 0.275 mm) within the cables. The resulting DIC FOV was about 15 mm, while the IR FOV was about 85 mm.

After each experiment, the DIC images were analyzed using the commercially-available Vic-3D software (Correlated Solutions, 2010), generating a large amount of data per experiment (roughly 25 GB). Each individual wire in the cables was assigned its own region of interest (ROI), centered on the crown of the wire, where the correlation analysis was performed. A single ROI was never chosen across multiple wires, because spurious strains would result due to wires moving past each other. In DIC, a small subset of the deformed image is matched to a small subset of the reference image using a cross correlation function. We utilized Vic-3D's default function, the normalized sum of squared differences (Sutton et al., 2009). The subset size was chosen using the "3-by-3" rule (3×3 pixels per speckle with 3×3 speckles per subset), as recommended by Sutton et al. (2009). In general, larger subsets lead to better correlation between the reference image and the deformed image, but subsets that are too large can result in "over-smoothing" of the strain fields, because Vic-3D assumes constant strain across the subset. Thus, the choice of subset size is a tradeoff between the correlation strength and the desired spatial resolution of strain inhomogeneities to be resolved. Subset size ranged between 23×23 and 19×19 pixels for different specimens, in order to include roughly 3×3 speckles inside each subset. To achieve a fine field resolution, an analysis grid spacing of either 1 or 2 pixels (about 6 to 12 μm) was used, where the 19×19 box (subset) was shifted by 1 or 2 pixels on a rectangular grid between each subset correlation. Once all subsets were correlated, the 3D displacements, their gradients, and selected strain components were calculated.

Line elements on the cable surfaces can undergo significant rotations, so it was important to chose a finite strain measure for the DIC data rather than the engineering (small) strain tensor $\boldsymbol{\varepsilon}$. $\mathbf{E}^{\mathrm{L}}$ and $\boldsymbol{\varepsilon}$ are equivalent for infinitesimal strains and rotations, but a small difference exists between these strain measures for the moderate strains in these experiments ($\approx 4\%$ to 8%). All mechanical responses are reported using the engineering strain measure by the LE (δ_e/L_e). The different between this and the averaged Green–Lagrange strain between the LE tags is $\overline{E}^{\mathrm{L}}_{zz} - \delta_e/L_e = 1/2\,(\delta_e/L_e)^2 \approx 0.08\%$ to 0.32% strain, so the relative error is $\overline{E}^{\mathrm{L}}_{zz}/(\delta_e/L_e) - 1 = 1/2(\delta_e/L_e) \approx 2\%$ to 4%. This small difference is acceptable for our purposes, since $\mathbf{E}^{\mathrm{L}}$ field measurements are primarily intended to track strain localizations.

5. Experimental results

Experimental results of the two cable designs are presented below in four subsections. Section 5.1 presents an initial comparison of the mechanical response of the two cables subjected to a single load-unload superelastic cycle. Sections 5.2 and 5.3 detail the strain and temperature responses, and Section 5.4 describes the multi-cycle shakedown behavior of the two cable designs. All experiments were performed at slow, nearly isothermal elongation rates. Part II of this series will present the slow-rate behavior of selected subcomponents of the two cables. A summary table of the experiments to be presented here is given in Table 2, showing the various specimens, dimensions, and experimental parameters. The experiment identifier starts with the type of specimen (C for cable, W for straight wire), then the cable/alloy type (1 for 7×7, 2 for 1×27), and then a lowercase letter appended for each experiment performed.

The average axial stress of each specimen is reported as P/A_0, where P is the tension force along the z-axis and $A_0 = n\pi d^2/4$ is a chosen reference area, based on the number of wires (n) in the specimen and the individual wire diameter (d). Note that this differs somewhat from the projected cross-sectional area of the wires (normal to the tensile axis), since the cross-section normals of most wires are misaligned to the cable axis. Circular wire cross-sections become projected approximately as ellipses[3] in the overall cable's cross-section. Nevertheless, the simple summation of wire cross-sections is a straightforward metric for reporting the macroscopic cable response and for later comparison with the response of a single straight wire.

The reaction torque, i.e., moment about the z-axis (M_z), generated by constraining the rotation of the specimen at the grips, is reported as $M_z R/J_0$, where R is the radius from the center of the specimen to the outermost point in the cross-section, and J_0 is a chosen reference torsion constant. One will recognize $\tau = M_z R/J_0$ as the classical formula for the maximum shear stress at the outer radius of a linearly elastic, straight, cylindrical rod subjected to twisting about its axis. Our torsion constant was selected simply as the polar moment of inertia of an idealized (fictitious) cross-section calculated by

$$J_0 = n\frac{\pi d^4}{32} + \sum_{i=1}^{n} \frac{\pi d^2}{4} r_i^2, \tag{1}$$

where the first term is the contribution of individual wires about their own axes and the second term is the sum of the parallel axis theorem contributions. Here, i is the index of the wire, r_i is the mean radius from the central z-axis of the specimen to the wire's center-

[3] The intersection of a helical wire with a plane z =constant is not quite an ellipse due to the wire curvature and its finite thickness, especially for tightly wound wires with small spring indices ($Ci \equiv r_i/r_w \simeq \mathcal{O}(1)$, where r_i and r_w are the nominal helix radius and wire cross-section radius, respectively).

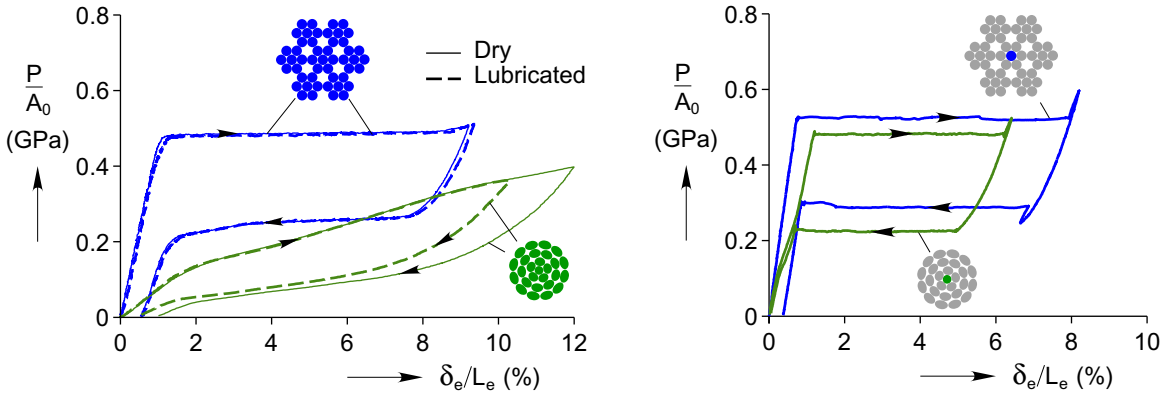

(a) Normalized force-LE strain for full cables (b) Stress-LE strain for core wires

Fig. 6. (a) Superelastic tension responses of the 7×7 (Experiments C1a and C1b) and 1×27 (Experiments C2a and C2b) cables. (b) Superelastic tension responses of the straight core wires extracted from the two cables (first cycle of Experiments W1a and W2a). Note that specimen lubrication does not have any appreciable effect on either of the cable responses, so further experiments were performed on dry specimens.

line, and wire cross-sections are treated as circles rather than ellipses. While the elementary theory does not strictly apply here, J_0 was chosen for simplicity to give an approximate sense of the average normal stress versus shear stress contributions in the different cable and strand designs.

5.1. Initial comparison of the two cables

Fig. 6(a) shows the average axial stress versus LE strain of four experiments performed on the two cable designs. For each cable design one specimen was as-received (dry, solid line) and one was lubricated (dashed line). To have a controlled comparison the cables were not painted with speckles for these experiments and thus DIC was not performed. Each pair of dry/lubricated specimens was subjected to the same slow rate to avoid thermomechanical coupling effects in room temperature air ($\dot{\delta}/L = \pm 2.5 \times 10^{-5}$ s^{-1} for both 7×7 specimens and $\dot{\delta}/L = \pm 1 \times 10^{-4}$ s^{-1} for both 1×27 specimens). Prior to the experiments shown by dashed lines, 7×7 and 1×27 cable specimens were immersed in penetrating lubricant (Grignard TN-3, composed of a non-petroleum group of synthetic di-esters) for 1 min. Following each experiment, the lubricated specimens were disassembled to confirm that the lubricant penetrated to the core.

Fig. 6(a) addresses whether specimen lubrication has an appreciable effect on a cable's mechanical response, and the answer is No. The figure shows a near exact match [4] between the lubricated and dry responses, which suggests that static friction between the wires was quite high and prevented relative sliding of subcomponents. This is consistent with (Costello, 1998), who devotes an entire chapter of his book on Wire Rope to argue that kinetic friction is a small effect in linear elastic cables. In the case of the single 1×27 strand, the argument is simple. If the entire strand is to stretch uniformly, the helical line of contact between the core wire and helical wires also stretches uniformly, so negligible relative motion exists between the core and helical wires. This indeed seems to be the case for the 1×27 cable, where the loading responses of the lubricated and dry specimens are virtually identical. The 7×7 cable has additional complications due to the motion of propagating fronts that may not be the same from wire to wire, as will be seen in Section 5.2. Nevertheless, the effect of lubrication is still barely noticeable, so further experiments were all performed on dry specimens.

[4] While the loading responses of the 1×27 specimens match quite well, the unloading responses are (of course) different since unloading began at different maximum strains in the two experiments.

For reference, Fig. 6(b) provides the uniaxial tension responses of the straight core wires that were removed from the respective cables. Both wires are superelastic at room temperature, but the mechanical responses are not identical. The 7×7 core wire has a larger loading plateau stress (526 MPa versus 481 MPa), a larger plateau strain (7.2% versus 5.0%, during loading), and a narrower stress hysteresis (238 MPa versus 260 MPa) compared to the 1×27 core wire. Also, the initial nonlinearity near 0.5% during loading in the 1×27 core wire response, yet absent from the 7×7 core wire response, is due to a stress-induced R-phase transformation. As shown in Miyazaki and Otsuka (1986), certain NiTi alloys exhibit a two stage transformation ($A \rightarrow R^+$ followed by $R^+ \rightarrow M^+$) when tested 10–20 °C above their A_f temperature, but the same alloys only show a single stage transformation ($A \rightarrow M^+$) when tested at higher temperatures.

Comparing the dry 7×7 cable response in Fig. 6(a) to that of its core wire in Fig. 6(b), the cable response is similar to that of a single superelastic wire in pure tension, since the force has been divided by the cross sectional area of all 49 wires. It has distinct loading and unloading plateaus commonly found in NiTi wires, which suggest the presence of propagating transformation fronts. Although the cable was strained to $\delta_e/L_e = 9.3\%$, just beyond the loading plateau, most of this deformation was recovered with only 0.5% residual strain remaining after unloading. The tensile load P was 1.42 kN (319 lbf) on the upper plateau. These characteristics should be encouraging for engineers wishing to leverage the excellent properties of SMA wire into a flexible, compact form that can withstand relatively large forces.

The 1×27 cable response, on the other hand, is significantly different from the typical uniaxial behavior of its SMA wires. The 1×27 cable response is nonlinear with a slight knee near 2% strain, but it has no obvious load plateau, i.e., it maintains a positive tangent modulus throughout loading–unloading. Also, no upturn in tangent modulus is seen, even by the maximum gage strain of $\delta_e/L_e = 12\%$. Here, a reduced axial force and a more compliant behavior has been traded for a larger recovery strain of about 11%, with a final residual strain of about 1%. In handling, the 1×27 specimen is also quite flexible in bending due to its larger helix angles that avoids direct tension/compression along the axis of the individual wires.

Thus, a wide range of cable behaviors can be achieved by simply varying the construction, which represents an opportunity for engineers to tailor the response to match the desired characteristics of specific applications. In particular, the 7×7 design might be desirable where a high initial stiffness is needed, yet distinct

load plateaus would be used to mitigate overload conditions or act as a mechanical switch. The 1×27 might be appropriate for applications where a larger recoverable stroke and increased bending compliance are needed and/or a more stable axial response is desired.

5.2. Details of the 7×7 cable response

Fig. 7 shows the mechanical response during Experiment C1c on a 7×7 specimen. Experiment C1c was performed on a similar cable to Experiments C1a and C1b, shown in Fig. 6, but at a displacement rate 2.5 times slower ($\dot{\delta}/L = \pm 1 \times 10^{-5}\ \mathrm{s}^{-1}$ versus $\dot{\delta}/L = \pm 2.5 \times 10^{-5}\ \mathrm{s}^{-1}$). Fig. 7(a) shows the mechanical response versus LE strain in terms of the normalized axial load (P/A_0, left axis) and normalized axial torque reaction ($M_z R/J_0$, right axis). Figs. 7(b) and (c) show the histories of average axial strains and the mechanical reactions against a common time axis. Fig. 7(b) shows the average strain derived from the grip displacement (δ/L, dashed line), which was controlled as a simple up-down ramp over the experiment duration of 20.5 ks (5.7 h). The evolution of the LE strain (δ_e/L_e, solid line) is also shown, which deviates from δ/L for reasons discussed below. Fig. 7(c) shows the corresponding time histories of normalized load (P/A_0) and normalized axial torque ($M_z R/J_0$).

The axial load-LE strain response shown for Experiment C1c in Fig. 7(a) is quite similar to those shown for C1a and C1b in Fig. 6, but now also shows the axial torque. The initial (austenite) axial load response of the 7×7 cable is nearly linear up to $\delta_e/L_e = 1.1\%$ with a modulus of $E_A = 45.5$ GPa. The upper (loading) plateau stress is 493 MPa with a strain extent of 8.66%. The lower (unloading) plateau stress is about 262 MPa, but the plateau is flat only between LE strains of 7.4% to 5.3% and the subsequent stress decreases gently until 1.5% strain, the onset of the final linear elastic unload segment.

Interestingly, the torque response in Fig. 7a during loading is non-monotonic. It initially exhibits a stiff linear branch with a slope of 13.5 GPa (shear stress/axial strain) up to a maximum torque at $\delta_e/L_e = 1.1\%$. This is interrupted at the onset of the axial load plateau by a softening branch in the torque response. Once the axial load plateau is completed at $\delta_e/L_e = 8.66\%$, the torque turns upward again slightly. Note that what appears to be a "nucleation peak" in the torque response during loading near $\delta_e/L_e = 1.1\%$ is actually an artifact of plotting the response against δ_e/L_e. As shown in Fig. 7(b), the global strain ramps linearly with time, but at the onset of the loading plateau the LE strain history is relatively static then suddenly rises more steeply at 4.8 ks. As will be shown later, this is due to propagating fronts that first traverse the specimen outside the LE gage section then later enter the LE section. As seen in Fig. 7(c), the "nucleation peak" disappears when the torque is plotted against the time, and the torque decreases almost linearly during the axial load plateau. The final residual strain is $\delta/L = 1.16\%$ by the grip displacement, but is only $\delta_e/L_e = 0.71\%$ by the LE measurement. The difference is likely due to some grip slippage that occurred during the experiment, a common issue in tension experiments on straight SMA specimens (not dog-bone specimens) that exhibit strain localization. Thus, local extensometer measurements are a more accurate representation of the material response, even if they can be more difficult to interpret in the presence of localized strain fields. For this reason, we chose to report δ_e/L_e in Fig. 7(a) instead of δ/L.

The IR temperature and DIC axial strain fields in the 7×7 cable during this experiment are shown in Fig. 8 and Fig. 9, respectively, and both indicate the presence of propagating transformation fronts. The temperature legend in Fig. 8 spans a 2 °C window near room temperature ($T_a \approx 21$ °C). The contour plot, $T(z,t)$, was created by taking IR images at 5 s intervals, extracting a vertical temperature distribution along the crown of the specimen in each image, stacking the resulting sequence of one pixel wide slices side-by-side, and synchronizing them with time. Since the laser tags have a much lower emissivity than the painted specimen, they are clearly visible in Fig. 8 as the prominent, but artificial, horizontal streaks. The IR temperature reading is inaccurate there, but the tags do provide good markers for the movement of those locations. In addition, the slight horizontal streak in the temperature field history at $z/L = 0.46$ is due to the specimen thermocouple. Throughout this paper and Part II, each IR contour plot includes a

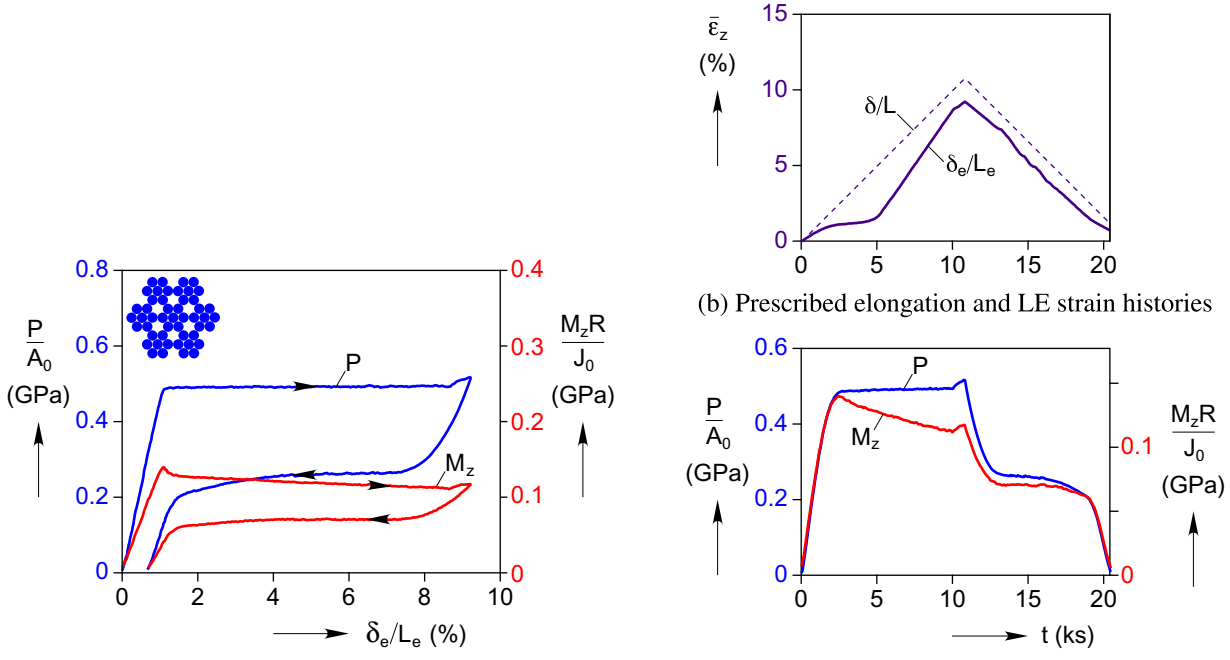

Fig. 7. Experiment C1c on 7×7 cable at $\dot{\delta}/L = \pm 1 \times 10^{-5}\ \mathrm{s}^{-1}$.

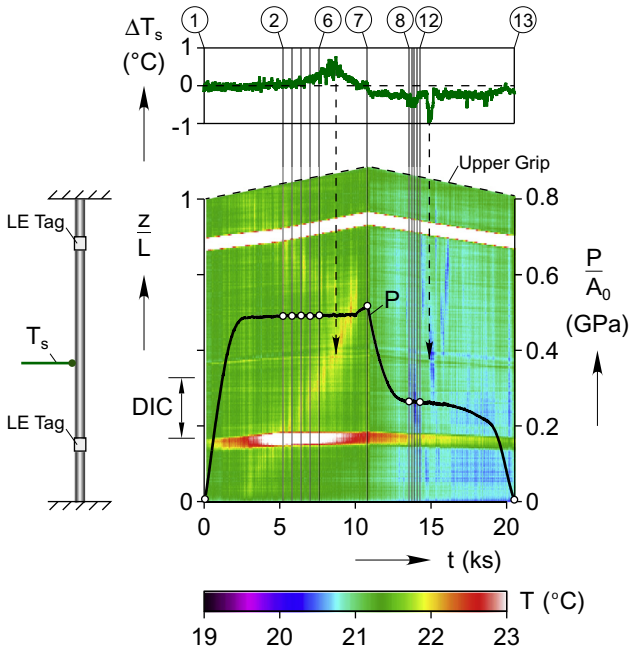

Fig. 8. Experiment C1c (7×7 cable at $\dot{\delta}/L = \pm 1 \times 10^{-5}\ s^{-1}$). IR temperature field (contour plot), normalized force (overlaid), and specimen thermocouple (above) histories. The labels above the specimen thermocouple history correspond to the DIC images in Fig. 9. A scaled schematic of the specimen reference configuration is shown to the left of the IR temperature plot. The $A \rightarrow M^+$ transformation appears in the temperature field history as two hot spots ($A \rightarrow M^+$ fronts) propagating inwards from the grips during loading, but the $M^+ \rightarrow A$ transformation is more diffuse upon unloading, with no clear fronts.

scaled schematic of the specimen at the left, showing the positions of LE tags and the thermocouple along the reference specimen length. Disregarding these locations, the overall kinetics of $A \rightarrow M^+$ transformation appear as two propagating hot spots, one from each grip, propagating inward and coalescing at $z/L = 0.68$ where the temperature reaches as high as 1.5 °C above ambient. Close inspection reveals that the fronts often appear to propagate in an alternating stop-start fashion, resulting in the vertical hot spot streaks in the contour plot. Each time the bottom front moves and heats up, the top front stops and cools down, and vice versa. During unloading, the kinetics of $M^+ \rightarrow A$ transformation are more diffuse without any clear fronts, just a few scattered local drops in temperature.

The time history of the temperature difference between the specimen and ambient thermocouples ($\Delta T_s \equiv T_s - T_a$, the topmost plot in Fig. 8) agrees well with the temperature field history. The noisy ΔT_s signal was due, in part, to the specimen thermocouple rubbing against the irregular surface of the cable as it deformed. Nevertheless, it recorded a small, but discernible, temperature peak near $t = 8.72$ ks of about 0.5 °C as $A \rightarrow M^+$ transformation occurred at the thermocouple location, and then a temperature drop of about -1 °C near $t = 14.89$ ks due to $M^+ \rightarrow A$ transformation. The vertical arrows in the contour plot show how the temperature peak/drop line up with instances when transformation activity was detected by the thermocouple.

The axial strain fields in Fig. 9 from the DIC analysis provide a magnified view of the front propagation. The images depict the strain field, $E^L_{zz}(x, z; t)$, at selected times corresponding to the upper labels and points overlaid on the stress history in Fig. 8. The images were taken in a restricted FOV of the specimen as indicated in Fig. 8. Each axial strain field was superimposed on a photograph of the cable in its current configuration, and colored according to the 0 to 10% strain legend for E^L_{zz}. The lower LE tag, which was initially out of view in ①, appears as a gray band in the bottom of each strain field image from times ② to ⑬. Overall, the DIC sequence shows a macroscopic $A \rightarrow M^+$ front propagating upward from the bottom grip during loading (③ to ⑥ in the FOV) with a distinct strain discontinuity from about 1% to 7.5% strain, and then a more diffuse global front moving downward during unloading (⑨ to ⑫). Although not obvious in the few DIC images shown, a video of the complete set of 343 images (at 60 s intervals) during loading shows the global front move, slow down, and then speed up again. This is consistent with the observation from the IR temperature field evolution that the fronts in the top half (beyond the DIC FOV) and bottom half of the specimen often propagate in an alternating start-stop manner.

Consistent with the IR imaging, the strain field images are more diffuse during unloading than during loading. In addition, the time interval between ⑧ to ⑫ during unloading is only 0.72 ks, much shorter than the time interval of 2.42 ks between ② to ⑥ during loading. As seen in the stress history of Fig. 8, ⑧ to ⑫ corresponds to the brief period where the axial load was constant. The front

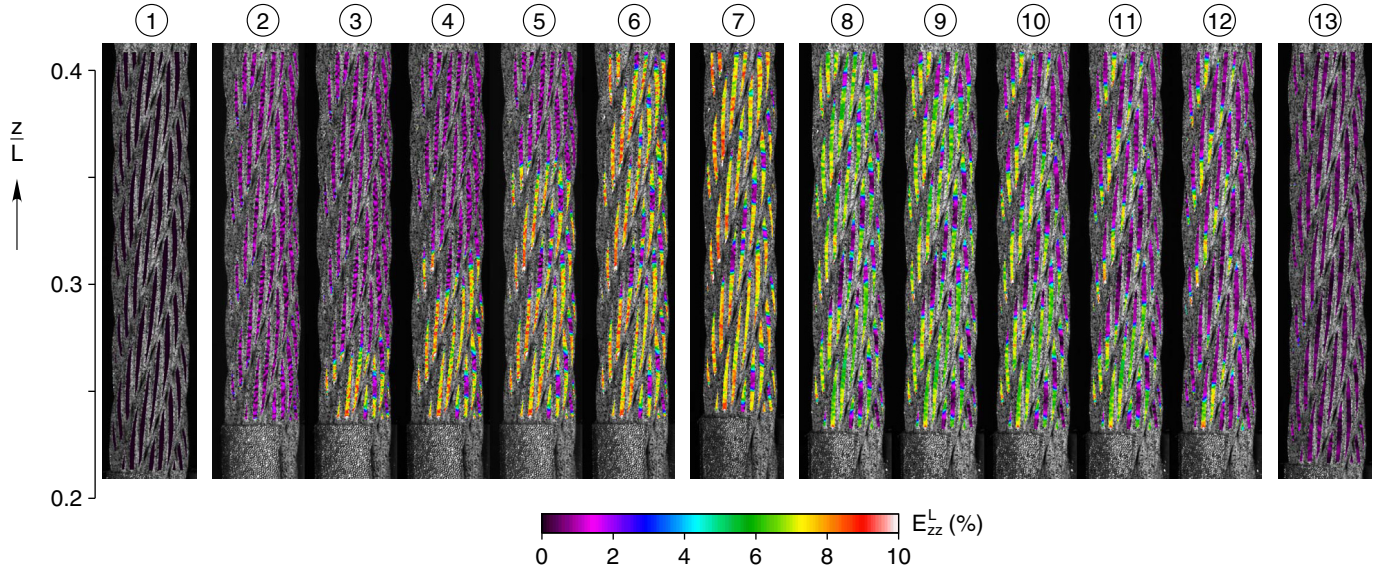

Fig. 9. Experiment C1c (7×7 cable at $\dot{\delta}/L = \pm 1 \times 10^{-5}\ s^{-1}$). DIC axial strain field images which correspond to the labels in Fig. 8. The strain field images provide a magnified view of the front propagation seen in Fig. 8. Note that certain individual wires in the cable do not completely transform as the global $A \rightarrow M^+$ front passes through.

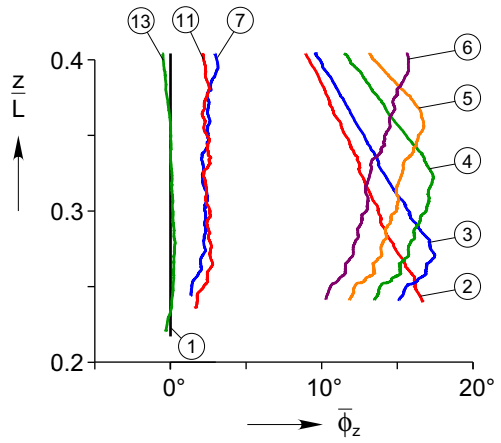

Fig. 10. Experiment C1c: Profiles of cross-section rotation about the z-axis of the 7×7 cable obtained by DIC analysis. The rotation field is relatively uniform until a global transformation front passes the DIC FOV (images ②–⑥), at which point the rotation increases substantially and a propagating kink appears.

traversal is much quicker during unloading, indicating a smaller transformation strain across the $M^+ \rightarrow A$ front. Further reverse transformation occurs in disparate regions and is accompanied by an overall decreasing axial stress history. Note that the fronts reach the grips well before the steep decrease in stress at $t = 19$ ks, which indicates the termination of $M^+ \rightarrow A$ transformation. Since most of the $M^+ \rightarrow A$ transformation occurs in a rather uniform manner, little temperature change is detected in the IR images during unloading. All of this behavior is probably due to shakedown and residual pockets of "locked-in" martensite in the NiTi wires (to be discussed further in Section 5.4), which may explain why most of the $M^+ \rightarrow A$ transformation required a decreasing load history.

The macroscopic front consists of fine features, first at the strand scale and then at the individual wire scale. The global front is jagged according to where fronts are located in the individual wires. These wire fronts tend to be staggered, which is reasonable since adjacent fronts would tend to amplify self-heating and would be energetically unfavorable. In other words, individual wire fronts tend to "repel" each other thermally, yet the steep local strain gradient along an individual wire's axis tends to encourage further transformation there.

Note that some of the individual wires in the cable do not completely transform as the global $A \rightarrow M^+$ front passes through a given region (see images ② to ⑥). The likely reason the exterior wires only partially transform is to maintain axial compatibility with the core strand. As the outer six strands of the cable stretch, they can also reduce their helix angles to accommodate a given global axial strain. The core strand must simply stretch, making the tensile strains in the core wires greater for the same global axial strain. The overall morphology of transformation must maintain global axial strain compatibility between the rigid grips, yet high friction between the components within the cable section also tends to enforce local axial strain compatibility between components. One can imagine that the radial compressive stresses are likely quite large between the outer helical strands and the core strand, since if unsupported the helical strands would contract radially inward (as for a simple tension coil spring taken to large strains). Once the loading plateau is exhausted ($t = 10.0$ to 10.8 ks), these low strain (austenite) regions shrink slightly (images ⑥ to ⑦). As will be seen in Part II, the end of the core strand plateau corresponds to the upturn in stress at the end of the 7×7 cable plateau. At this point the outer strands have not yet fully exhausted their loading plateaus. Only when the core strand begins to uniformly strain again after the termination of

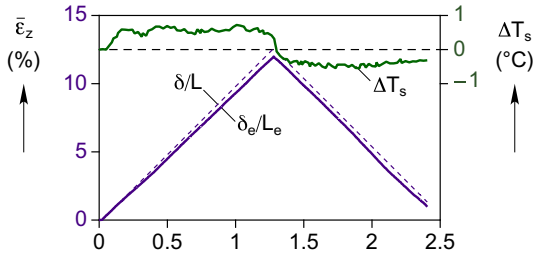

(b) Prescribed elongation, LE strain, and thermocouple histories

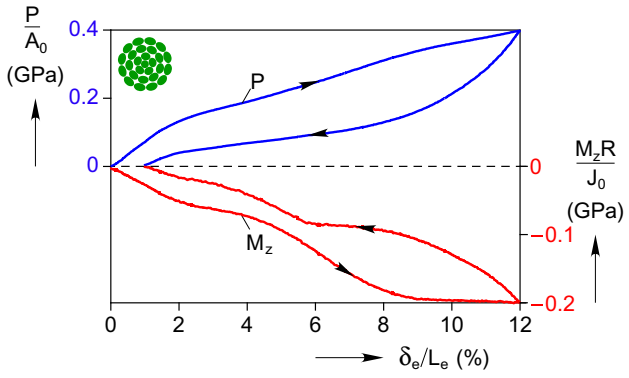

(a) Normalized axial force and torque versus LE strain

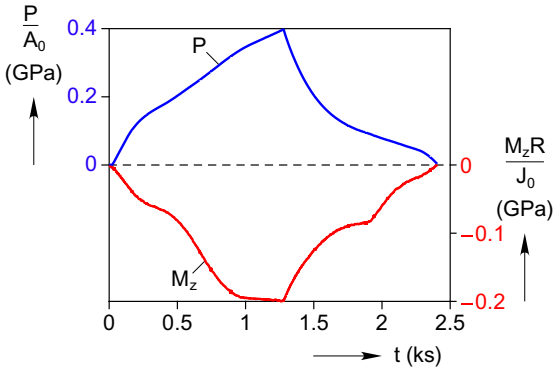

(c) Normalized axial force and torque histories

Fig. 11. Experiment C2a (1×27 cable at $\dot{\delta}/L = \pm 1 \times 10^{-4}$ s^{-1}). The torque magnitude in (a) of the 1×27 cable is significantly larger than that of the 7×7 cable due to the much larger helix angles of the 1×27 wires. Unlike the 7×7 cable response, the LE strain in (b) follows the prescribed elongation closely, and the specimen thermocouple records step-like changes in time, both indicating the absence of localized transformation.

its plateau do the pockets of austenite in the exterior strands begin to disappear.

Another interesting observation is that cable cross-sections rotate about the z-axis. A cable made of conventional stable material, restrained from rotation at the grips, would not exhibit this behavior. Selected cross-section rotation profiles ($\bar{\phi}_z(z)$, in a right-hand sense) in the DIC FOV are shown in Fig. 10. These were obtained by (1) fitting a cylinder to the DIC data points to determine the precise location of the z-axis for a cylindrical coordinate system, (2) subtracting the current angle of each material point from the angle at zero axial load to get $\phi_z(\theta, z)$, then (3) averaging across the cable diameter to obtain an average angle, $\bar{\phi}_z(z)$, for each cross section. Fig. 10 shows that whenever the strain field is relatively uniform, such as between time $t = 0.02$ ks (①) and $t = 2.5$ ks (just prior to $A \rightarrow M^+$ transformation) and ⑦ to ⑬ (unloading), the cable rotation is relatively constant along the length and is less than 4°. However, as the macroscopic front traverses the DIC FOV, ② to ⑥, a kink exists in the rotation profile with a propagating peak (reaching as high as 17.5° in ③), whose location corresponds to the position of the global front. Upon subsequent unloading where localized deformation is less prevalent, the rotation at ⑦ is about 2.3°, and there is little change between ⑦ to ⑪. After final unloading at ⑬ the rotation is essentially zero again.

5.3. Details of the 1×27 cable response

We now turn to Experiment C2a performed on a 1×27 cable specimen at $\dot{\delta}/L = \pm 1 \times 10^{-4}\ \mathrm{s}^{-1}$. The mechanical response is shown in Fig. 11(a) in terms of the axial load and axial torque versus LE strain. The axial load response is the one shown previously in Fig. 6 (dry).

Relative to its axial load, the torque magnitude of the 1×27 cable is significantly larger than that of the 7×7 cable. The increase in relative torque magnitude is due to the much larger helix angles of the 1×27 wires, despite the alternating lays in the construction. The 1×27 torque is negative according to the right-hand sign convention adopted in Fig. 4(a), and during loading it exhibits an interesting multi-step behavior with a knee at about 2% strain and another knee at about 8% strain. These undulations will be shown in Part II to be due to transformation activity in the individual layers of the cross-section occurring at different times.

Histories of the average axial strains and specimen thermocouple in Experiment C2a (Fig. 11b) show no evidence of propagating transformation fronts. First, in contrast to the 7×7 cable, the 1×27 grip and LE strain histories match more closely. There is a small amount of grip slippage, but the LE strain traces nearly constant-rate ramps. Second, recall that the 7×7 cable specimen thermocouple measured sharp temperature increases and decreases as the transformation front passed by the thermocouple (topmost portion of Fig. 8). The 1×27 specimen thermocouple history, on the other hand, indicates a more constant rate of heating/cooling during loading/unloading, without any sharp peaks indicative of localized propagating heat sources/sinks.

The specimen thermocouple measurements also suggest that the 1×27 is less rate sensitive. During loading/unloading, the thermocouple measured a rise/drop in temperature of about ±0.5 °C. These deviations from the ambient temperature are roughly the same magnitudes as seen in the previous experiment on the 7×7 cable, despite the $10 \times$ faster elongation rate. The reduced rate sensitivity is due to several factors, including the lack of propagating transformation fronts, the deeper helix angles in the construction, and the somewhat more slender aspect ratio. A further study of these factors, as well as experiments at higher rates, can be found in Reedlunn (2011).

5.4. Cyclic shakedown responses

Most SMAs exhibit an evolution of their thermo-mechanical response during their first thermo-mechanical cycles. This process is called *shakedown* if the response asymptotically approaches a limit cycle. Since repeatable cyclic behavior is often essential for the success of an SMA device, cyclic shakedown is an important aspect to characterize. In practice, the material may be subjected to 'training' to achieve a repeatable limit-cycle behavior, which additionally may be used to induce a two-way shape memory effect. The degree and cyclic rate of shakedown are strongly dependent on the particular training procedure used and have obvious implications for durability and fatigue life. Despite intense interest in the literature e.g. (Bo and Lagoudas, 1999; Eggeler et al., 2004; Churchill and Shaw, 2008; Kan and Kang, 2010), a comprehensive map of the influence of possible training procedures does not yet exist even for monolithic SMAs, due to the large variety of loading parameters (temperature, strain, stress) and their path dependence. Accordingly, the purpose of this section is to preliminarily explore the different cyclic responses of the two cable designs.

Before presenting the cyclic responses of the cables and attempting a comparison, the early shakedown responses of the straight core wires extracted from the two cables is shown to establish the base material differences. The responses to six cycles for each core wire are shown in Fig. 12. The force–elongation responses for the 7×7 and 1×27 core wires are shown respectively in Fig. 12(a) (Experiment W1a) and Fig. 12(c) (Experiment W2a), each subjected to six load-unload cycles taken to a maximum strain just beyond its load plateau. The corresponding stress and specimen temperature histories are shown in Figs. 12(b) and (d).

Focussing first on Fig. 12(a), the evolution of the superelastic response of the $7 \times 7 \times 0.275$ mm core wire is shown for six cycles to a maximum LE strain of 8.15%. The cyclic response shows how the superelastic response progresses from one that has distinct plateaus (first cycle, $N = 1$) to one that has a more sigmoid-like shape (last cycle, $N = 6$). During this process, the upper plateau moves downward in stress and the lower plateau moves downward to a lesser degree, until a flat plateau is no longer discernible during either $A \rightarrow M^+$ or $M^+ \rightarrow A$. The length of both plateaus decrease and eventually develop a positive tangent modulus, while the strain and temperature fields tend to become more uniform (although not shown here). As cycling proceeds, the magnitude of the hysteresis (area within the loop) diminishes. The residual strain, upon each unloading to zero axial load, evolves forward in strain (ratchets) with progressively smaller increments after cycle 2. Interestingly, the increment of residual strain accumulation after cycle 2 is actually larger than after cycle 1, but decreases monotonically thereafter. The final residual strain after cycle 6 is 2.74%. This is only one specific example, relevant to the study at hand, and more cycles would be required to truly reach a limit cycle behavior.

The specimen thermocouple history of the 7×7 core wire in Fig. 12(b) indicates the transition from distinct transformation fronts toward spatially diffuse transformations. Fig. 12(b) shows both the specimen temperature changes, as measured by a thermocouple placed near the bottom laser tag, and the axial stress history for reference. The temperature excursions are about ±0.6 °C during cycles 1 and 2 and are relatively sharp in time (≈ 150 s duration), indicating localized transformation as transformation fronts pass the thermocouple location. A final sharp peak is measured during cycle 4 at 6 ks, which is due to a new nucleation event. Subsequently, however, the temperature changes become progressively rounded and diminished in magnitude to roughly ±0.1 °C by cycle 6, indicating more diffuse transformations. As expected, this change in temperature behavior corresponds to the disappearance of the stress plateaus.

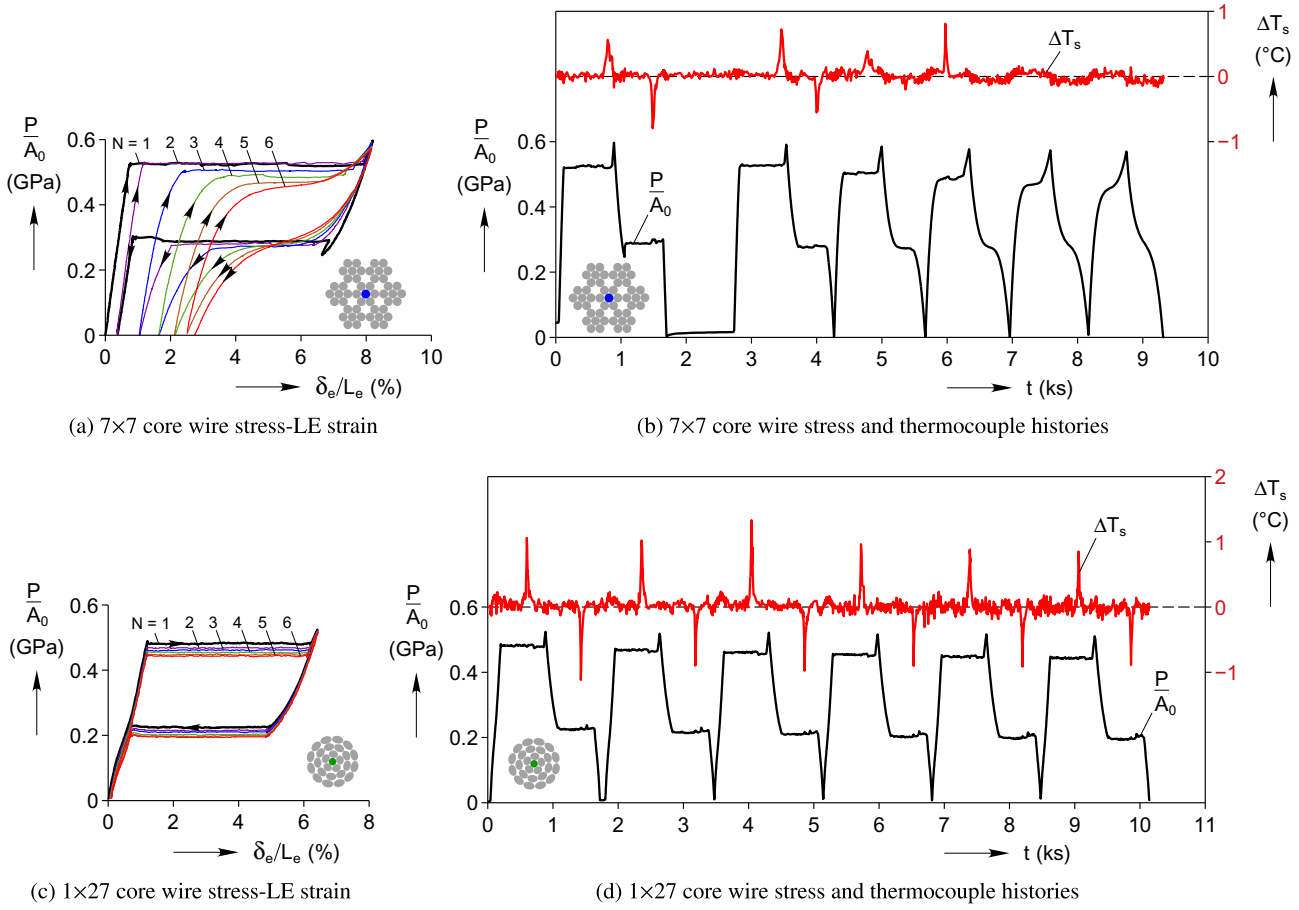

(a) 7×7 core wire stress-LE strain

(b) 7×7 core wire stress and thermocouple histories

(c) 1×27 core wire stress-LE strain

(d) 1×27 core wire stress and thermocouple histories

Fig. 12. Superelastic cyclic responses at $\dot{\delta}/L = \pm 1 \times 10^{-4}\ s^{-1}$ (Experiments W1a and W2a) of the straight core wires extracted from the two cables. The 1×27 core wire stress–strain response in (a) shows less severe shakedown than the 7×7 core wire in (c). Furthermore, unlike the 7×7 core wire in (b), the 1×27 core wire temperature history in (d) shows temporal spikes in the specimen temperature for all six cycles. These spikes, and the flat stress plateaus in (c), indicate persistent $R^+ \leftrightarrow M^+$ transformation fronts in the 1×27 core wire during cycling.

In contrast to the 7×7 core wire, Fig. 12(c) shows a less severe shakedown in the mechanical response of the 1×27 core wire. The stress plateaus remain over the six cycles but just shift downward somewhat in each cycle (about -35 MPa in total). The residual strain even after cycle 6 is only 0.1%, and the superelastic loop remains nearly closed. Fig. 12(d) shows that, unlike the 7×7 core wire, the temporal spikes in specimen temperature exist for all six cycles. Both this feature and the flatness of the stress plateaus indicate that phase transformations still involve propagating fronts.

Clearly the alloys are not identical, which is unfortunate for a direct comparison between the two cables. We suspect processing variables for the two cable constructions were varied, leading to the different material properties. As shown in the DSC thermograms of Fig. 3, we estimate that the 1×27 wire is superelastic above 10 °C, while the 7×7 wire is superelastic above -24 °C. This difference causes the 1×27 wire to have a -45 MPa lower loading plateau stress and a -64 MPa lower unloading plateau stress in the first cycle. Because the plateau strain is also smaller for the 1×27 wire, the maximum strain during cycling was less (6.41% vs. 8.19%). Generally speaking, the cyclic rate of shakedown (if ever reached) is quite sensitive to the transformation stress, and thus to the specimen temperature according to the Clausius–Clapeyron relation. The shakedown evolution is also indirectly sensitive to the maximum strain, especially if taken well beyond the initial loading plateau. Had we taken the 1×27 wire to the same maximum strain as the 7×7 wire, which would have been well into the post-plateau regime, the shakedown would have been more severe.

The mechanical response of the full 7×7 cable (Exp. C1d) during cycling (Fig. 13(a)) is qualitatively similar to that of its core wire (Fig. 12(a)). To reduce the duration of this longer experiment (Exp. C1d) the elongation rate was $\dot{\delta}/L = \pm 1 \times 10^{-4}\ s^{-1}$, ten times faster than the previous 7×7 cable experiment (C1c). This rate is still rather slow, however, and is the same rate used in the cyclic core wire experiment (Exp. W1a). The maximum strain during each cycle on the 7×7 cable was $\delta_e/L_e = 10.37\%$, just beyond the initial load plateau as shown in Fig. 13(a). In the first cycle of the 7×7 cable, after the initial stiff, nearly linear, mechanical response, there exist the usual distinct plateaus during loading ($A \rightarrow M^+$ transformation) and unloading ($M^+ \rightarrow A$ transformation). The subsequent cycles exhibit the typical superelastic shakedown response for NiTi when stress-induced transformation requires a large stress (over 500 MPa in this case). Similar to the core wire response, the mechanical response becomes more sigmoid-like as cycling proceeds, and the magnitude of the hysteresis (area within the loop) diminishes. At the same time, the strain at zero stress increases, but in successively smaller increments for each cycle (again after cycle 2). Comparing cycle 1 and 6 of the 7×7 cable, the incremental changes with cycles are qualitatively similar to that of the core wire (Fig. 12(a)), but the changes are larger for the cable specimen.

The cyclic evolution of the 7×7 cable specimen thermocouple readings follow the same general trend shown for its core wire in Fig. 12(b), but quantitative differences do exist. First, the temperature peaks during the first cycle occur over about 1000 s, indicating that transformation in the cable is more diffuse than in the core

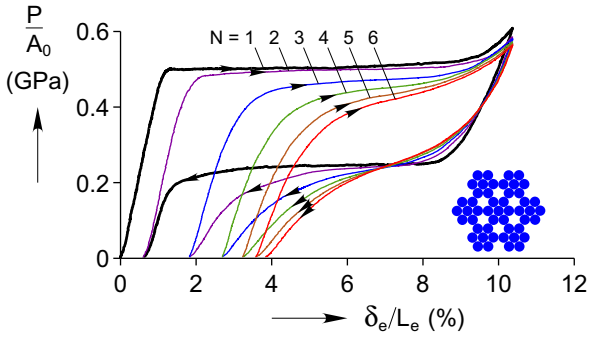

(a) Normalized force-LE strain

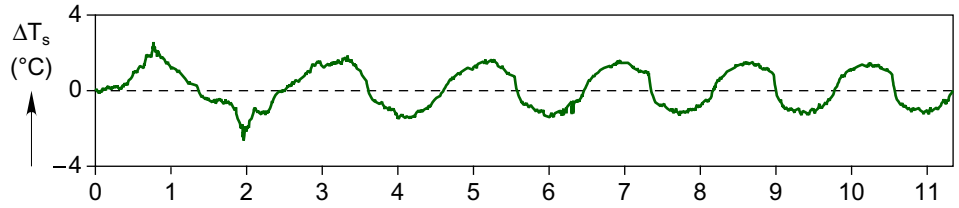

(b) Specimen thermocouple history

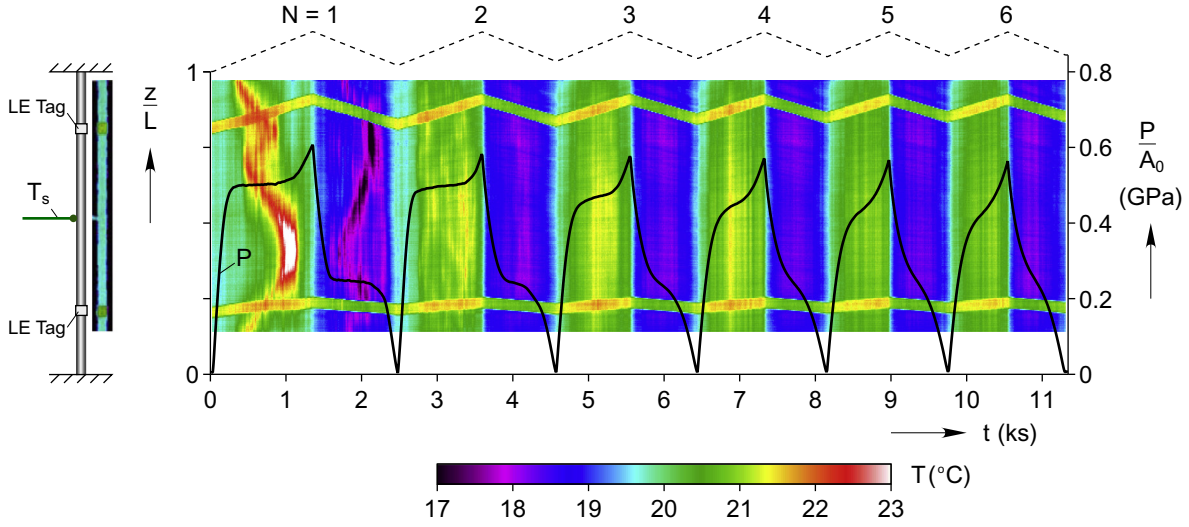

(c) IR temperature field (contour plot) and normalized force (overlaid) histories

Fig. 13. Experiment C1d (6 cycles of a 7×7 specimen at $\dot{\delta}/L = \pm 1 \times 10^{-4}\ \mathrm{s}^{-1}$). Consistent with the cyclic evolution of the mechanical response in (a), well-defined transformation fronts are clearly visible only during the first cycle in (c), with transformations exhibiting progressively more uniform temperature profiles during subsequent cycling. Compared to its core wire (Fig. 12(b)), the full cable's temperature response shows larger temperature excursions (due to the larger thermal scaling) and more diffuse transformations, both spatially and temporally.

wire. Second, the magnitudes of the temperature excursion are larger in the cable for the same global strain rate (note the different temperature scales). In cycle 1, the temperature excursions are ±2.5 °C, which fades to ±1.4 °C by cycle 6. This larger temperature change is due to the larger thermal scaling (volume/exposed surface area ratio) of the cable, despite the more diffuse transformation in the cable compared to the wire.

The 7×7 cable IR contour plot (Fig. 13(c)) clearly shows localized transformation front activity during the first cycle. The FOV of the IR camera in this experiment includes most, but not all, of the free length, and the grayscale legend spans 6 °C about ambient room temperature (20 °C). During the first cycle, as expected from the flat loading and unloading plateaus, the temperature field shows transformation fronts traversing the specimen gage length (again ignore the LE tag locations). One front nucleates at the top grip and another front nucleates at the bottom grip, due to the stress concentrations there. Once the temperature of the initial two fronts rises by about 2.2 °C, another pair of fronts nucleate at $z/L = 0.7$. The top two fronts, one from the top grip, the other from the $z/L = 0.7$ nucleation, coalesce at $z/L = 0.8$, at which point a very small drop in the load was measured at $t = 0.85$ ks. This leaves only the bottom two fronts, which speed up to comply with the global strain rate $\dot{\delta}/L = \pm 1 \times 10^{-4}\ \mathrm{s}^{-1}$, thereby raising the local exothermic heat release rate. As these fronts propagate and approach each other, they thermally interact, locally raising the temperature to 24.7 °C, above the limit of the temperature scale in the figure, when they coalesce at $z/L = 0.4$. The temperature rise is accompanied by a 22 MPa increase in propagation stress. After

the fronts coalesce, the specimen temperature does not immediately return to room temperature (cyan). Instead, the specimen remains above ambient by about 1 °C. In fact, the upper edge of the IR FOV that had briefly cooled to room temperature, heats up again when the axial load takes its upturn after the plateau. During this time, a vertical 21 °C band is observed across the entire FOV, which is likely due to the regions of austenite shown in images ③–⑦ of Fig. 9, which were left behind by the global front, finally transforming to martensite. We do not have DIC data for this experiment to prove the point, but given that the uniform heating occurs between $\delta_e/L_e = 8.8\%$ and 10.2%, and the remnant regions of austenite started to transform at $\delta_e/L_e = 8.7\%$ in the isothermal DIC experiment, we are confident this is the case. During the unloading plateau, two fronts emanate from the final coalescent site during loading, and close inspection reveals evidence of transformation activity near the other coalescent site as well (cool spots near $z/L = 0.75$ at $t = 1.6$ ks). Reverse nucleations at the site of $A \rightarrow M^+$ front coalescences are commonly observed in uniaxially loaded wires (Chang et al., 2006), so the observation here is not surprising. The two $M^+ \rightarrow A$ fronts from $z/L = 0.4$ propagate outward until they meet fronts emanating from the grips at $z/L = 0.25$ and 0.8, and the temperature drops low off-scale (black) in those regions. After these four $M^+ \rightarrow A$ fronts coalesce, and some further transformation occurs scattered along the gage length, reverse transformation completes and the specimen returns to zero load.

During cycles 2–6, transformation activity in the 7×7 cable becomes more dispersed and eventually becomes nearly uniform. While the specimen thermocouple history in Fig. 13(b) recorded sharp temporal peaks during the first cycle, the peaks become more rounded and reduced in magnitude as cycling progresses. Likewise, the IR contour plot shows well defined transformation front propagation during the first cycle, but the temperature excursions becomes rather scattered and reduced in magnitude during subsequent cycles. Some local transformation activity is detected during the loading portion of the second cycle, but it occurs in an uncoordinated fashion and no clear propagating fronts are apparent. Transformation fronts likely exist in individual wires or groups of wires, yet transformation seems to be nucleating at several locations with relatively little room for propagation. During cycles 3 through 6, a temperature rise and fall are still measured during each $A \rightarrow M^+$ and $M^+ \rightarrow A$ transformation, respectively, but the magnitudes become progressively reduced and eventually become nearly spatially uniform. Following the stress history in Fig. 13(a), the loading segment of the second cycle still has a relatively flat, but gently rising, loading plateau, while some local transformation activity is evident in the IR temperature field. However, once the temperature field becomes more uniform, as in cycles 3–6, the stress history becomes more sigmoid-like in shape.

The final experiment (C2c) of this paper is shown in Fig. 14, showing that cyclic shakedown in the 1×27 cable is less severe than in the 7×7 cable. The 1×27 cable was subjected to six load-unload cycles at the same rate ($\dot{\delta}/L = \pm 1 \times 10^{-4}$ s^{-1}), but the maximum strain was larger ($\delta_e/L_e = 12.5\%$). Fig. 14(a) shows the evolution of the mechanical response, where the qualitative shape of the response does not change significantly with cycling. While the mechanical response is certainly nonlinear and has gentle undulations, it never exhibits a distinct plateau even during its first cycle. The residual strain only ratcheted to δ_e/L_e =2.0% and a limit cycle (complete shakedown) was nearly reached by cycle 6. By contrast, the 7×7 cable residual strain reached 4% by cycle 6, despite being cycled to a smaller maximum strain (δ_e/L_e =10.3%). Furthermore, the shape of the 7×7 cable mechanical response changed dramatically during the first six cycles, and the response would certainly continue to evolve after cycle 6, unlike the 1×27 cable.

As expected from the mechanical response of the 1×27 cable that never exhibited load plateaus, the IR temperature field (Fig. 14(c)) and specimen thermocouple temperature history (Fig. 14(b)) show no evidence of propagating transformation fronts. The IR temperature field plot does show exothermic temperature changes during each loading and endothermic temperature changes during unloading, but the temperature profiles are rather uniform at any given time, at least in the central FOV of the IR camera. Likewise, the thermocouple history lacks any sharp peaks, instead measuring up or down step-like temperature changes depending on the sign of the elongation rate, $\dot{\delta}$. Over the six cycles, the temperature deviations from ambient during loading and unloading (about ±1.5 °C) do not change significantly, as opposed to the 7×7 design whose temperature deviations became smaller with each successive cycle.

As a final comparison, certain features of the cyclic mechanical responses of the two cables are compared in Fig. 15. Characteristic stresses at the onset and termination of the plateaus, or knees, in the response curves are shown in Fig. 15(a) and 15(b) for the respective cables. The insets in the figures show the constructions used to extract these stresses from the mechanical response (final cycle response shown) in a systematic way. For the 7×7 cable, Fig. 15(a) shows that stresses at the onset/termination of the $A \rightarrow M^+$ plateau generally decrease with cycles, but diverge from each other as the response curve becomes more sigmoid-like. The stresses during the $M^+ \rightarrow A$ plateau also diverge from each other, but the onset of the knee moves upward in stress while the reverse knee near the termination of $M^+ \rightarrow A$ transformation moves downward. The average of these two values remains relatively constant with cycling. The cyclic trends in each value are relatively monotonic, and the dotted lines are single-exponential fits of the data (for $N \geqslant 2$) as discussed further below. The trends in the characteristic stresses for the 1×27 cable in Fig. 15(b) are less dramatic. The first knee in the curve, which indicates the onset of transformation to M^+, quickly converges to an asymptotic value by about cycle 3. The other three characteristic stresses change very little over the six cycles.

Fig. 15(c) plots the residual strains upon complete unloading after each cycle, and Fig. 15(d) plots the initial and final elastic moduli for each cycle. The dashed lines are exponential fits that nicely capture the trends of the data, at least for these few cycles. For example, we chose the form $\varepsilon_r(N) = \varepsilon_r^\infty \left[1 - \exp\left(-\frac{N-N_0}{\tau}\right)\right]$ for the residual strain fits. Fig. 15c clearly shows the more extreme evolution of the residual strain for the 7×7 cable with a predicted asymptotic value of about 4.3% strain, compared to the 1×27 cable which has a predicted asymptotic value of about 2.3% strain. Interestingly, the data fits in Fig. 15(c) do not extrapolate to the origin as one might expect, again showing that the first cycle is somewhat of an outlier in the overall cyclic trends in the mechanical response (as it was for the straight wire). Likewise, the trends in Fig. 15(d) show a significantly reduced elastic modulus for the 7×7 cable, but very little change in elastic modulus for the 1×27 cable.

The exponential-like behavior (starting with the second cycle) in all these features suggests that their evolution may be governed by a Maxwellian "rate" equation. For example, suppose the characteristic stresses are each governed by the first-order differential equation

$$\frac{d\sigma}{dN} = -\frac{\sigma}{\tau}, \tag{2}$$

where τ is a "time-constant" in terms of the number of full transformation cycles the material experiences. This has the exponential solution

$$\Delta\sigma(N) = \Delta\sigma_\infty \left[1 - \exp\left(-\frac{N}{\tau}\right)\right], \tag{3}$$

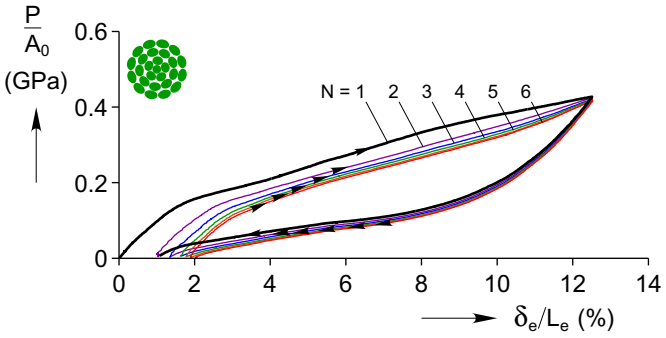

(a) Normalized force-LE strain

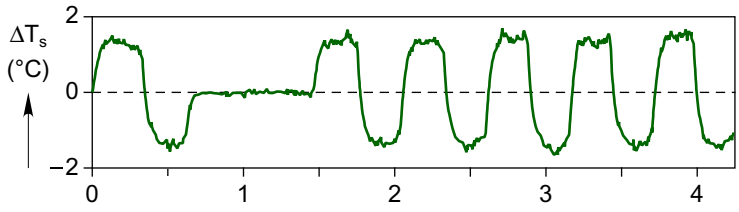

(b) Specimen thermocouple history

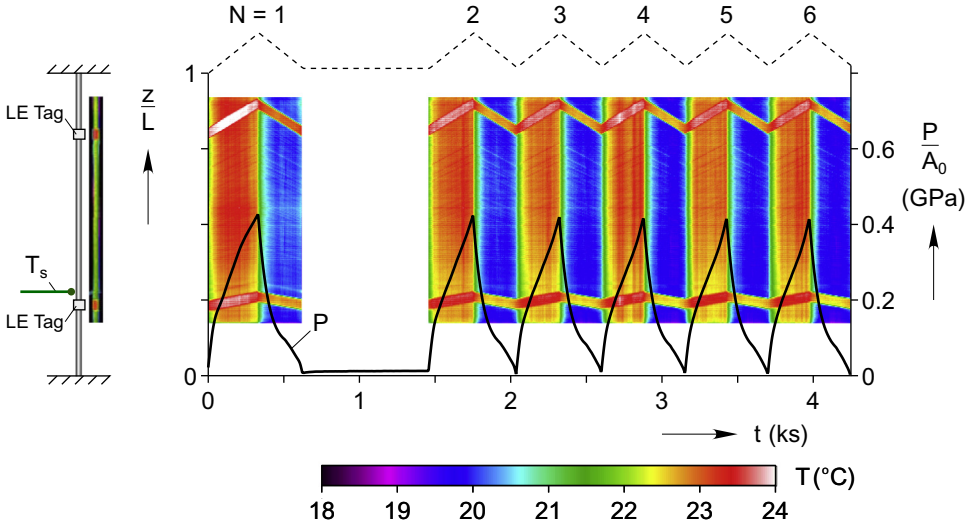

(c) IR temperature field (contour plot) and normalized force (overlaid) histories

Fig. 14. Experiment C2c (six cycles of a 1×27 cable at $\dot{\delta}/L = \pm 4 \times 10^{-4}\ s^{-1}$). The 1×27 cable response exhibits relatively mild shakedown in (a), and the uniform temperature fields in (c) at each time instant confirm the absence of propagating transformation fronts.

where $\Delta\sigma(N)$ is the change in the transformation stress from its initial value, and $\Delta\sigma_\infty$ is the asymptotic (shaken down) change after a sufficiently large number of cycles. We suspect the cyclic "rate-constant" (τ) during shakedown is determined more by the material and the temperature at which the experiment was run, than by the construction of the cable. The amount of shakedown ($\Delta\sigma_\infty$), however, is probably a strong function of the cable construction, since it influences the distribution and multi-axiality of the local stress state in the wires.

Of course, the maximum strains between the two experiments are different, so a direct comparison here is difficult. Furthermore, as shown previously in Fig. 12, the two cable designs were constructed from somewhat different NiTi alloys so it is not possible to quantitatively determine how much of the difference in shakedown behavior is due to the cable design versus differences in material properties. We leave for later the challenging modeling task of determining shakedown in various cable constructions from the underlying cyclic constitutive behavior of its individual wires. Nevertheless, given the enhanced compliance of the 1×27 components and lack of propagating transformation fronts (in all but perhaps the single core wire), the cable construction certainly plays a significant role.

Overall, the data suggests the 1×27 cable may have better ultimate fatigue performance, durability, and overall high-cycle repeatability. Of course, this comes at the cost of a significantly reduced stiffness and less dramatic transitions between elastic and phase transformation regions, if those are desired. Thus, the question of which cable design is favored depends on the intended application. It should be apparent by now that many other possible constructions could be investigated to obtain behaviors in between, or drastically different, from those shown here.

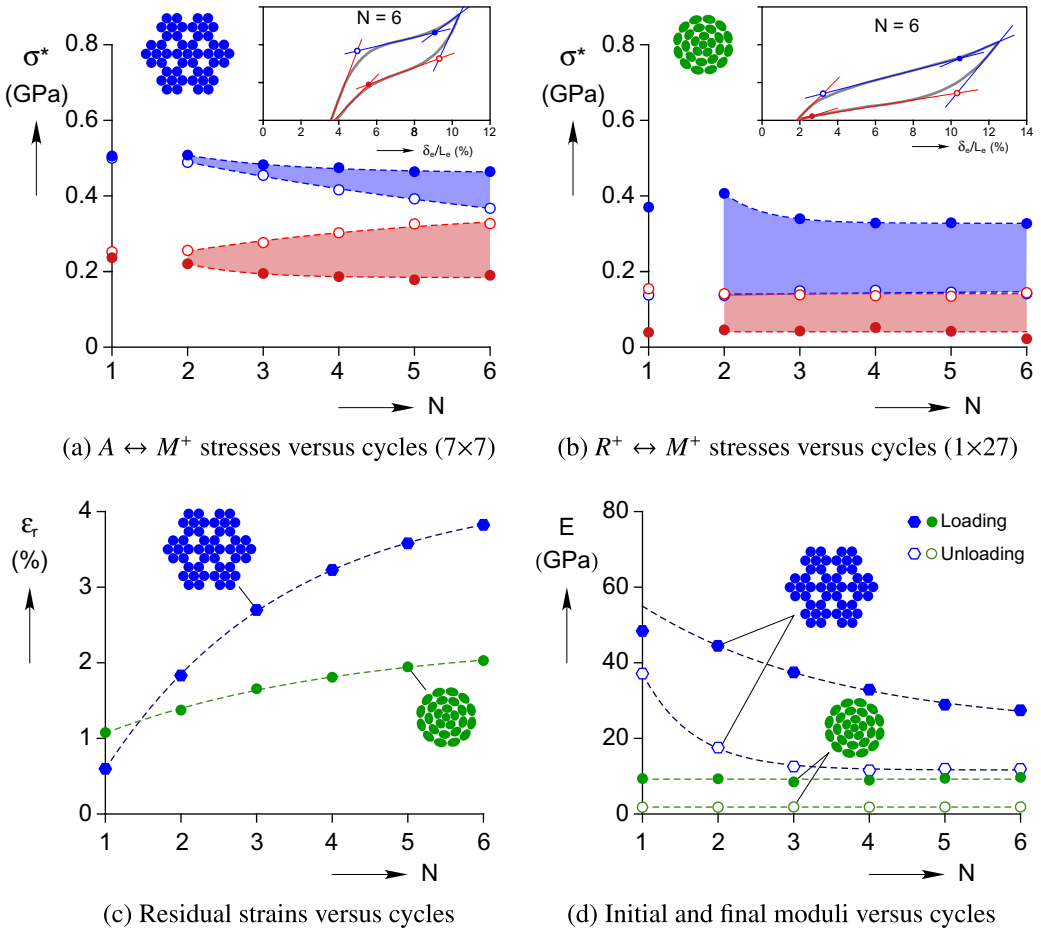

Fig. 15. Comparison of the cyclic evolution of 7 × 7 and 1 × 27 cable responses, showing (a) and (b) characteristic transformation stresses, (c) residual strains, and (d) initial loading modulus (closed symbols) and unloading modulus (open symbols). These again show a more dramatic cyclic evolution of response features in the 7 × 7 cable than in the 1 × 27 cable.

6. Summary and conclusions

The room temperature, nearly isothermal tensile responses of the 7 × 7 × 0.275 mm cable and 1 × 27 × 0.226 mm cable were characterized. Both cable design responses were relatively unaffected by lubrication, indicating high friction between the subcomponents. Overall, the mechanical responses of the 7 × 7 cable and the straight core wire extracted from it were quite similar, indicating the 7 × 7 cable behaves similar to that of 49 straight wires loaded in parallel. The behavior of the 1 × 27 cable was considerably different due to the larger helix angles involved in its construction. Thus, the 7 × 7 cable may be ideal for those engineers wishing to exploit the excellent properties of superelastic wires in a high force, compact package, while the 1 × 27 cable trades off force for a larger recoverable strain, exhibits a more stable structural response with a positive tangent modulus, and less severe shakedown characteristics. Both cables had an interesting non-monotonic torque reaction during the tension experiments, yet the relative magnitude was more significant in the 1 × 27 cable due to the larger helix angles in its construction.

Simultaneous infrared thermography and stereo digital image correlation were used during the experiments on the two designs to investigate the local strain and temperature field variations. The 7 × 7 cable clearly exhibited propagating phase transformation fronts that behaved in a similar manner to the fronts in its straight core wire. Some interesting features were observed, however, in the propagation of fronts between adjacent wires in the cable and some incomplete propagation in some of the outermost wires. Stress-induced phase transformation activity was detected in the temperature fields of the 1 × 27, but no propagating transformation fronts were observed. This made the 1 × 27 specimen less sensitive to latent heat-induced temperature changes, allowing relatively isothermal experiments to be performed at faster elongation rates than for the 7 × 7 cable. The range of responses for the two cable designs seems to indicate significant future opportunities to tailor the structural behavior of SMA cables to their intended applications by designing the construction and layups.

Part II that follows will study the response of selected subcomponents excised from the two cable constructions to asses the individual contributions of the cables' hierarchical construction.

7. Acknowledgements

We gratefully acknowledge the financial support for this work, provided by General Motors Research and Development through the GM/UM Collaborative Research Laboratory (CRL) in Smart Materials and Structures, the National Science Foundation (CMMI-0727331), and the US Department of Energy, Office of Basic Energy Sciences (DE-SC0003996). Helpful discussions with the members of the GM/UM CRL throughout the course of this work are acknowledged. Specimen materials were provided by Fort Wayne Metals Research at no cost, along with helpful guidance, which are also very much appreciated.

References

Barooah, P., Rey, N., 2002. Closed-loop control of a shape memory alloy actuation system for variable area fan nozzle. In: Rao, V.S. (Ed.), Proceedings of SPIE, pp. 384–395.

Bo, Z., Lagoudas, D., 1999. Thermomechanical modeling of polycrystalline SMAs under cyclic loading. Part III: Evolution of plastic strains and two-way shape memory effect. International Journal of Engineering Science 37, 1175–1203.

Chang, B.C., Shaw, J.A., Iadicola, M.A., 2006. Thermodynamics of shape memory alloy wire: modeling, experiments, and application. Continuum Mechanics and Thermodynamics 18, 83–118.

Churchill, C.B., Shaw, J.A., 2008. Shakedown response of conditioned shape memory alloy wire. In: Behavior and Mechanics of Multifunctional and Composite Materials, Proceedings of the SPIE 15th Annual International Symposium on Smart Structures and Materials, p. 6929F.

Correlated Solutions, 2010. Vic-3D Manual. Correlated Solutions, Inc. Columbia, SC.

Costello, G., 1998. Theory of Wire Rope. Springer, NY, second ed..

DesRoches, R., McCormick, J., 2003. Properties of large diameter shape memory alloys under cyclical loading. Proceedings of SPIE – The International Society for Optical Engineering 5057, 187–196.

Duerig, T.W., Melton, K.N., Stöckel, D., Wayman, C.M. (Eds.), 1990. Engineering Aspects of Shape Memory Alloys. Butterworth-Heinemann, Boston, MA.

Eggeler, G., Hornbogen, E., Yawny, A., Heckmann, A., Wagner, M., 2004. Structural and functional fatigue of niti shape memory alloys. Materials Science Engineering A – Structure 378, 24–33.

Frick, C.P., Ortega, A.M., Tyber, J., Maksound, A.E.M., Maier, H.J., Liu, Y., Gall, K., 2005. Thermal processing of polycrystalline NiTi shape memory alloys. Materials Science and Engineering: A 405, 34–49.

Ft. Wayne Metals, 2010. Personal communication. <http://www.fwmetals.com/strands.php>.

Ft. Wayne Metals, 2012. Personal communication. <http://www.fwmetals.com/strands.php>.

Funakubo, H., 1987. Shape Memory Alloys. Gordon and Breach Science Publishers, NY.

Grummon, D., Shaw, J., Foltz, J., 2006. Fabrication of cellular shape memory alloy materials by reactive eutectic brazing using niobium. Materials Science and Engineering, A, 1113–1118.

Huber, J., Fleck, N., Ashby, M., 1997. The selection of mechanical actuators based on performance indices. Proceedings of the Royal Society of London, Series A 453, 2185–2205.

Kan, Q., Kang, G., 2010. Constitutive model for uniaxial transformation ratchetting of super-elastic niti shape memory alloy at room temperature. International Journal of Plasticity 26, 441–465.

Liu, Y., Liu, Y., Van-Humbeeck, J., 1998. Lüders-like deformation associated with martensite reorientation in NiTi. Scripta Materialia, vol. 39, pp. 1047–1055.

McKenna, H.A., Hearle, J.W.S., O'Hear, N., 2004. Handbook of Fibre Rope Technology. CRC Press, LLC.

Meier, B. 2007. <http://www.nytimes.com/2007/10/16/business/16device.html>.

Miyazaki, S., Otsuka, K., 1986. Deformation and transition behavior associated with the R-phase in Ti–Ni alloys. Metallurgical and Materials Transactions A 17, 53–63.

Ortega, A., Tyber, J., Frick, C., Gall, K., Maier, H., 2005. Cast NiTi shape-memory alloys. Advanced Engineeering Materials 7, 492–507, Germany.

Otsuka, K., Wayman, C.M., 1998. Shape Memory Materials. Cambridge University Press, Cambridge, UK.

Otsuka, K., Sawamura, T., Shimizu, K., 1971. Crystal structure and internal defects of equiatomic TiNi martensite. Physics State Solid (A) 5, 457.

Redmond, J.A., Brei, D., Luntz, J., Browne, A.L., Johnson, N.L., 2008. Behavioral model and experimental validation for a spool-packaged shape memory alloy actuator. In: Davis, L.P., Henderson, B.K., McMickell, M.B. (Eds.), In: Proceedings of SPIE, Industrial and Commercial Applications of Smart Structures Technologies 2008, SPIE. pp. 693004-69004-13.

Reedlunn, B., 2011. Thermomechanical Behavior of Shape Memory Alloy Cables and Tubes. PhD dissertation. The University of Michigan, Department of Mechanical Engineering.

Reedlunn, B., Shaw, J.A., 2008. Shape memory alloy cables, In: Dapino, M.J., Ounaies, Z. (Eds.), Proceedings of the SPIE 15th Annual International Symposium in Smart Structures and Materials, SPIE, p. 69291G.

Reedlunn, B., Shaw, J.A., Daly, S., 2009. Shape memory alloy cables: Exploratory experiments. In: Proceedings of the ASME Conference on Smart Materials, Adaptive Structures and Intelligent Systems (SMASIS 2009), ASME, pp. 149–160.

Reedlunn, B., Shaw, J., Daly, S., 2010. Pseudoelastic shape memory alloy cables. In: Grummon, D.S., Mitchell, M.R., Mertmann, M. (Eds.), Proceedings of the International Conference on Shape Memory and Superelastic Technologies (SMST 2010), ASM, Springer.

Reedlunn, B., Daly, S., Hector, L.G.J., Zavattieri, P., Shaw, J.A., 2013. Tips and tricks for characterizing shape memory alloy wire: Part 5 – full-field strain measurement by digital image correlation. Experimental Techniques 37.

Rey, N.M., Tillman, G., Miller, R.M., Wynosky, T., Larkin, M.J., Flamm, J.D., Bangert, L.S., 2001. Shape memory alloy actuation for a variable area fan nozzle. In: A.-M.R. McGowan (Ed.), Society of Photo-Optical Instrumentation Engineers (SPIE) Conference Series, pp. 371–382.

Semba, H., Okabe, N., Yamaji, T., Okita, K., Yamauchi, K., 2005. Axial compressive behavior of single-stage bellows of TiNi shape memory alloy for seismic applications. Materials Science Forum, 2055–2058.

Shaw, J.A., Kyriakides, S., 1995. Thermomechanical aspects of NiTi. Journal of the Mechanics and Physics of Solids 43, 1243–1281.

Shaw, J.A., Kyriakides, S., 1997. On the nucleation and propagation of phase transformation fronts in a NiTi alloy. Acta Materialia 45, 683–700.

Shaw, J.A., Kyriakides, S., 1998. Initiation and propagation of localized deformation in elasto–plastic strips under uniaxial tension. International Journal of Plasticity 13, 837–871.

Shaw, J.A., Grummon, D.S., Foltz, J., 2007. Superelastic NiTi honeycombs: fabrication and experiments. Smart Materials and Structures 16, S170–S178.

Shaw, J.A., Churchill, C.B., Iadicola, M.A., 2008. Tips and tricks for characterizing shape memory alloy wire: Part 1 – Differential scanning calorimetry and basic phenomena. Experimental Techniques, 55–62.

Song, G., Mo, Y.L., Otero, K., Gu, H., 2006. Health monitoring and rehabilitation of a concrete structure using intelligent materials. Smart Materials and Structures 15, 309–314.

Sun, Q.P., Li, Z.Q., Tse, K.K., 2000. On superelastic deformation of NiTi shape memory alloy micro-tubes and wires — band nucleation and propagation. In: Proceedings of IUTAM Symposium on Smart Structures and Structronic Systems, Magdeburg, Germany.

Sutton, M.A., Orteu, J.J., Schreier, H.W., 2009. Image Correlation for Shape, Motion, and Deformation Measurements: Basic Concepts, Theory, and Applications. Springer, New York.